

# Characterizing the Marginal Ice Zone in the Greenland Sea Through Seasonal Floe-Scale Sea Ice Observations

Daniel M. WATKINS,<sup>1</sup> Ellen M. BUCKLEY,<sup>2</sup> Minki KIM,<sup>1</sup> Jennifer K. HUTCHINGS,<sup>3</sup> Monica M. WILHELMUS<sup>1</sup>

<sup>1</sup>*Center for Fluid Mechanics, Brown University, Providence, RI, USA*

<sup>2</sup>*Department of Earth Science & Environmental Change, University of Illinois Urbana-Champaign,  
Urbana, IL, USA*

<sup>3</sup>*College of Earth, Ocean, and Atmospheric Sciences, Oregon State University, Corvallis, OR, USA*

*Correspondence:* Monica M. Wilhelmus <[mmwilhelmus@brown.edu](mailto:mmwilhelmus@brown.edu)>

**ABSTRACT.** Sea ice motion in the marginal ice zone (MIZ) is inherently multi-scale, influenced by the relationship between the floe size distribution (FSD) and the temporal and spatial scales of winds and ocean currents. Joint observations of the FSD and motion are necessary to develop and validate models of the MIZ. However, such observations are rare. We present observations of floe-scale Lagrangian sea ice translation and rotation in the East Greenland MIZ spanning the spring-to-summer transition for years 2003-20. The observations are derived from moderate-resolution optical imagery using the Ice Floe Tracker (IFT) algorithm and consist of floe shapes, geometric properties, and trajectories. We investigate FSD seasonality, links between floe size, translation, and rotation, and length scale dependence of horizontal deformation. The FSD evolves from April to July, with increasing prevalence of small floes. Variability of both drift speed and rotation depend on the floe size. Deformation rates show strong length scale dependence and vary seasonally. Comparisons to large-scale sea ice motion and to discrete element model simulations show that deviations from the mean drift resolved by IFT are exponentially distributed, suggesting ocean turbulence is resolved. These observations provide new information for sea ice model development and val-

28 idation in the MIZ.

29 **INTRODUCTION**

30 The size of an individual plate of ice—the *floe scale*—is foundational to sea ice dynamics in the marginal  
31 ice zone (MIZ). The relationship between the floe scale and the spatial scales of atmospheric and oceanic  
32 motion is important for understanding coupled interactions, as stresses from the atmosphere and ocean  
33 are integrated across the surface of the floe (Brenner and others, 2023; Gupta and others, 2024; Kim and  
34 others, 2024). The spacing between floes and the range of floe sizes in an area, characterized by the sea  
35 ice concentration (SIC) and the floe size distribution (FSD), respectively, strongly affect air-ocean fluxes,  
36 lateral melt rates, wave-ice interactions, and floe-floe interactions (McNutt and Overland, 2003; Loose and  
37 others, 2014; Roach and others, 2018; Wenta and Herman, 2018; Horvat, 2022; Herman, 2022; Manucharyan  
38 and others, 2022; Brenner and Horvat, 2024). Thus, joint observations of floe shapes and motion are needed  
39 to characterize MIZ sea ice dynamics.

40 Spatial and temporal variability in ice motion is directly related to the FSD and SIC (Overland and  
41 others, 1995; Dumont, 2022; Herman, 2022). The FSD is constantly evolving as floes either become larger  
42 due to pieces of ice interlocking, rafting, ridging and fusing, or smaller due to fracture and melt (Zhang  
43 and others, 2015; Horvat and others, 2016; Bateson and others, 2020; Roach and others, 2024). The tight  
44 coupling between the seasonally evolving FSD, mesoscale and submesoscale ocean currents, waves, and  
45 wind stress in the MIZ results in complex sea ice motion patterns with low spatial correlation (meters  
46 to kilometers) and short temporal scales (hours to days) (Thorndike and Colony, 1982; Hakkinen, 1987;  
47 Johannessen and others, 1987a,b; Feltham, 2005; Cole and others, 2017; Watkins and others, 2023)).

48 This complexity poses a challenge for sea ice observation and modeling. Sea ice motion is routinely  
49 monitored through drifting buoys and by processing remote sensing imagery (Webster and others, 2022;  
50 Gerland and others, 2019; Sandven and others, 2023). The physical processes that can be resolved by a  
51 particular sea ice observation system are constrained by the spatial resolution and acquisition frequency,  
52 as well as the reference frame of observations: buoys capture ice motion in a Lagrangian sense, whereas  
53 most remote sensing products produce Eulerian motion estimates. Outside dedicated experiments where  
54 multiple observation sources are merged (Uttal and others, 2002; Hwang and others, 2017; Rabe and others,  
55 2024, e.g.), few observation sources exist that jointly observe ice dynamics and floe properties.

56 Buoys track the motion of individual ice floes with high precision. At large scales (greater than 100 km),  
 57 operational buoy deployments through the International Arctic Buoy Program (IABP, Rigor and others  
 58 (2008)) provide long-term coverage. Due to the difficulty and expense of deployment, this data is spatially  
 59 and temporally sparse, particularly in the MIZ (Gerland and others, 2019; Brunette and others, 2022). In  
 60 addition, information on sea ice properties from buoys is limited to point-wise measurements. Hence the  
 61 representativeness of a buoy observation in space must be estimated, for example, through collation with  
 62 other sensors.

63 Remote sensing observations from satellites and aircraft enable observation of sea ice properties across  
 64 large spatial regions. Ice motion is estimated from satellite imagery by estimating the displacement of  
 65 sea ice from the shift in pixel intensity from one image to the next, for example through maximizing  
 66 cross-correlation (Ninnis and others, 1986; Kwok and others, 1998). For such methods, the motion vectors  
 67 produced represent an area-average within the spatial window used by the correlation algorithm. In the  
 68 pack ice, where spatial correlation is high, the sea ice moves coherently and displacement estimates have high  
 69 confidence; however, the same spatial window in the MIZ may include thousands of jostling floes, resulting  
 70 in higher uncertainty (Sumata and others, 2014; Gui and others, 2020). Moreover, many products are only  
 71 available seasonally, with few products providing estimates of motion during the summer melt season due  
 72 to the presence of liquid water at the snow and ice surface affecting the quality of the images and the  
 73 ability to distinguish between surface melt water and leads (Lavergne and others, 2010; Girard-Ardhuin  
 74 and Ezraty, 2012). Thus the representativeness, availability, and uncertainty of remote sensing-derived ice  
 75 motion vectors varies spatially and temporally, and is degraded in the MIZ.

76 In contrast to sea ice motion, the FSD is not routinely measured, though standard operational ice  
 77 charts do include information on predominant floe size categories (Dedrick and others, 2001; Afanasyeva  
 78 and others, 2019). To date, knowledge of the properties and variability of the FSD comes through individual  
 79 studies. Observation of the sea ice FSD from airborne remote sensing imagery dates back to Rothrock and  
 80 Thorndike (1984). Noting an approximately linear FSD probability density function (PDF) in log-log  
 81 space, they suggested characterization of the FSD via a power law with the form

$$82 \quad p(x) = cx^{-\alpha} \quad (1)$$

83 where  $x$  is a measure of floe size,  $c$  is a normalization constant and the parameter  $\alpha$  is the slope of the power  
 84 law distribution on a log-log scale. Numerous methods and image types have been used to characterize

the FSD (Paget and others, 2001; Toyota and others, 2006; Hwang, 2013). As a result, measured FSD properties (and methods) vary substantially across studies (Stern and others, 2018b), often showing a clear departure from Eq. 1. Note that the form of Eq. (1) is an empirical, not theoretical result (Herman, 2010), and distinct mechanisms governing the evolution of the FSD may lead to other forms of the FSD PDF. For example, theoretical and model-based analyses of floe breakup through wave action suggest a log-normal FSD (Montiel and Mokus, 2022; Mokus and Montiel, 2022).

Development and validation of models capable of simulating small-scale sea ice variability requires observations of sea ice across scales. Traditional models of sea ice dynamics and thermodynamics rely on a continuum approximation, with most current coupled climate models adopting a form of the viscous-plastic or elastic-viscous-plastic rheology (Hibler (1979), Hunke and Dukowicz (1997); see Tandon and others (2018); Hutter and others (2022); Zhang and others (2024) for tabulation of the sea ice schemes in modern Earth system models). Such models successfully reproduce many aspects of large-scale sea ice dynamics and thermodynamics (Hutter and others (2018); Zhang (2021)), but are not well suited to the scales of motion observed in MIZs (Herman, 2022). Observations of scale dependence in sea ice deformation using SAR-derived Lagrangian ice trajectories (Marsan and others, 2004; Stern and Lindsay, 2009) have motivated the development of alternative approaches, including the elastic anisotropic plastic (Tsamados and others, 2013; Heorton and others, 2018) and brittle rheologies (Girard and others, 2011; Rampal and others, 2016; Boutin and others, 2021; Ólason and others, 2022). Similar scale dependence has been described in buoy data by, e.g., Rampal and others (2008) and by Itkin and others (2017). Scale dependence varies spatially (Hutter and others, 2018), hence observations are needed from a wide range of locations and sea ice conditions.

Reconciling the levels of model complexity needed for large-scale climate simulations, local-scale forecasting, and process-level investigations of sea ice physics remains an active area of discussion (Blockley and others, 2020). The inclusion of FSD parameterizations in continuum models is seen as a potential path forward for better simulation of small scale thermodynamic and dynamic sea ice processes and wave-ice interactions (Zhang and others, 2015; Horvat and Tziperman, 2015; Roach and others, 2018; Bateson and others, 2020). Such parameterizations provide links between the statistics of the FSD and other sea ice processes, rather than explicitly representing ice floes. Alternatively, discrete element models (DEMs) include the effects of the FSD on ice motion either explicitly (disks, polygons, e.g. Gupta and others (2024); Damsgaard and others (2018); Brenner and others (2023); Manucharyan and Montemuro (2022))

115 or implicitly through bonded particles (Åström and Polojärvi, 2024). It is worth noting that the high  
116 computational cost of DEMs has historically limited their applicability to large-scale coupled Earth system  
117 models. Nonetheless, improved FSD parameterizations from additional observations have advanced the  
118 predictability of sea ice and will likely be important inclusions as computational abilities improve.

119 In this study, we present observations of floe-scale sea ice motion derived from optical satellite imagery.  
120 We focus on the Fram Strait and East Greenland ice tongue due to its importance as a connection between  
121 the Arctic and the world oceans (Smedsrød and others, 2017; Sumata and others, 2022), as it is the  
122 main passage of sea ice export from the Arctic Ocean. In addition, the presence of sharp gradients in  
123 the ocean currents and distinct mesoscale features affecting the ice dynamics (Manley, 1987; Kozlov and  
124 Atadzhanova, 2021; Morozov and Kozlov, 2023; Watkins and others, 2023) make it an ideal testbed for  
125 measuring complex, small-scale sea ice dynamics. Our observations aim to fill a major observational data  
126 gap for sea ice dynamics in the spring-to-summer MIZ. Floe shapes detected by the algorithm enable  
127 analysis of the sampling variability and seasonality of the FSD. The observations are presented alongside  
128 the results of a discrete element sea ice model simulation showing the effects of mesoscale and submesoscale  
129 eddy forcing on sea ice rotation and drift variability. We emphasize the effects of floe size on sea ice motion,  
130 including effects of an evolving FSD, proximity of the sea ice edge, and the presence of a rich upper ocean  
131 eddy field.

## 132 DATA

### 133 Sea ice segmentation and tracking

134 We obtain measurements of floe-scale sea ice motion derived from moderate resolution optical satellite  
135 imagery using the Ice Floe Tracker (IFT) algorithm (Lopez-Acosta and others, 2019). The study region  
136 covers the area northeast of Greenland from the Fram Strait in the north to Scoresby Sound in the  
137 south (Fig. 1, green box). The dataset consists of segmented satellite imagery, floe shape statistics, and  
138 derived floe trajectories. We first describe the source data, algorithm, and post-processing routines, then  
139 summarize the contents of the dataset. The full dataset is available at the Brown Digital Repository at  
140 <https://doi.org/10.26300/ydtf-e778>.

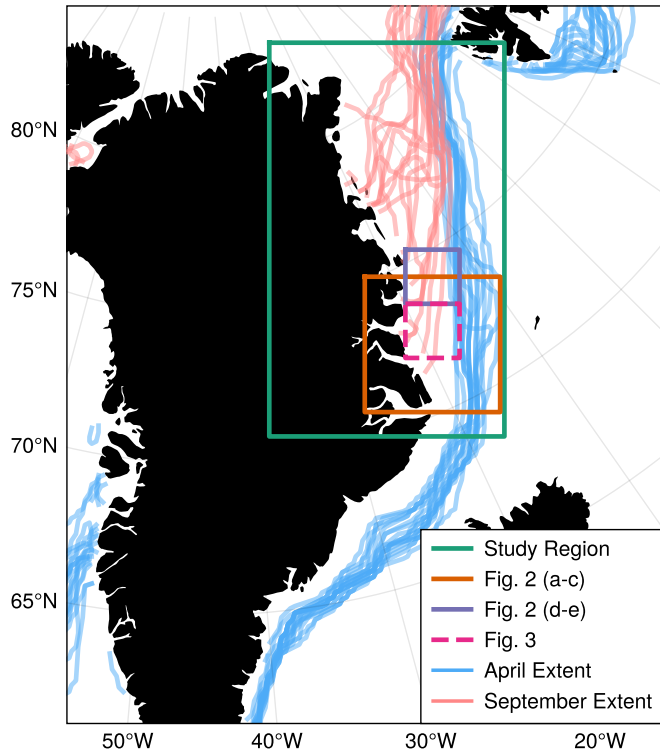


**Fig. 1.** Map of the study region (green box) and extent of image details for subsequent figures (solid orange, solid purple, and dashed pink boxes). Blue lines show the mean April sea ice extent for each year 2003-20, while pink lines show the September mean.

141 *Satellite imagery*

142 We acquired daily 250-m resolution true color (bands 1-3-4) and false color (bands 7-2-1) mosaic imagery  
 143 from the Moderate Resolution Imaging Spectroradiometer (MODIS) instruments via the NASA Worldview  
 144 Snapshots utility (Fig. 2a, b). Two images are used each day, corresponding to the daytime overpasses  
 145 of the Aqua and Terra satellites. Overpass times for the two satellites are generally between 20 and 90  
 146 minutes apart. Data are provided on a North Polar Stereographic grid. As imagery is only labeled with the  
 147 date, we use the Satellite Overpass Identification Tool (Hatcher and others, 2022) to identify the precise  
 148 overpass time for each image for use in ice motion calculations. We focused on the spring and summer  
 149 months (April 1 to September 15) to ensure consistent illumination, and cover years 2003-20. Sea ice in  
 150 the region has a large seasonal cycle and significant year-to-year variability. Blue and red lines in Fig. 2  
 151 mark the April and September mean sea ice extent for each year from the National Snow and Ice Data  
 152 Center (NSIDC) Sea Ice Index (Fetterer and others, 2017). The end-of-season ice extent exhibits greater  
 153 year-to-year variability than winter extent.

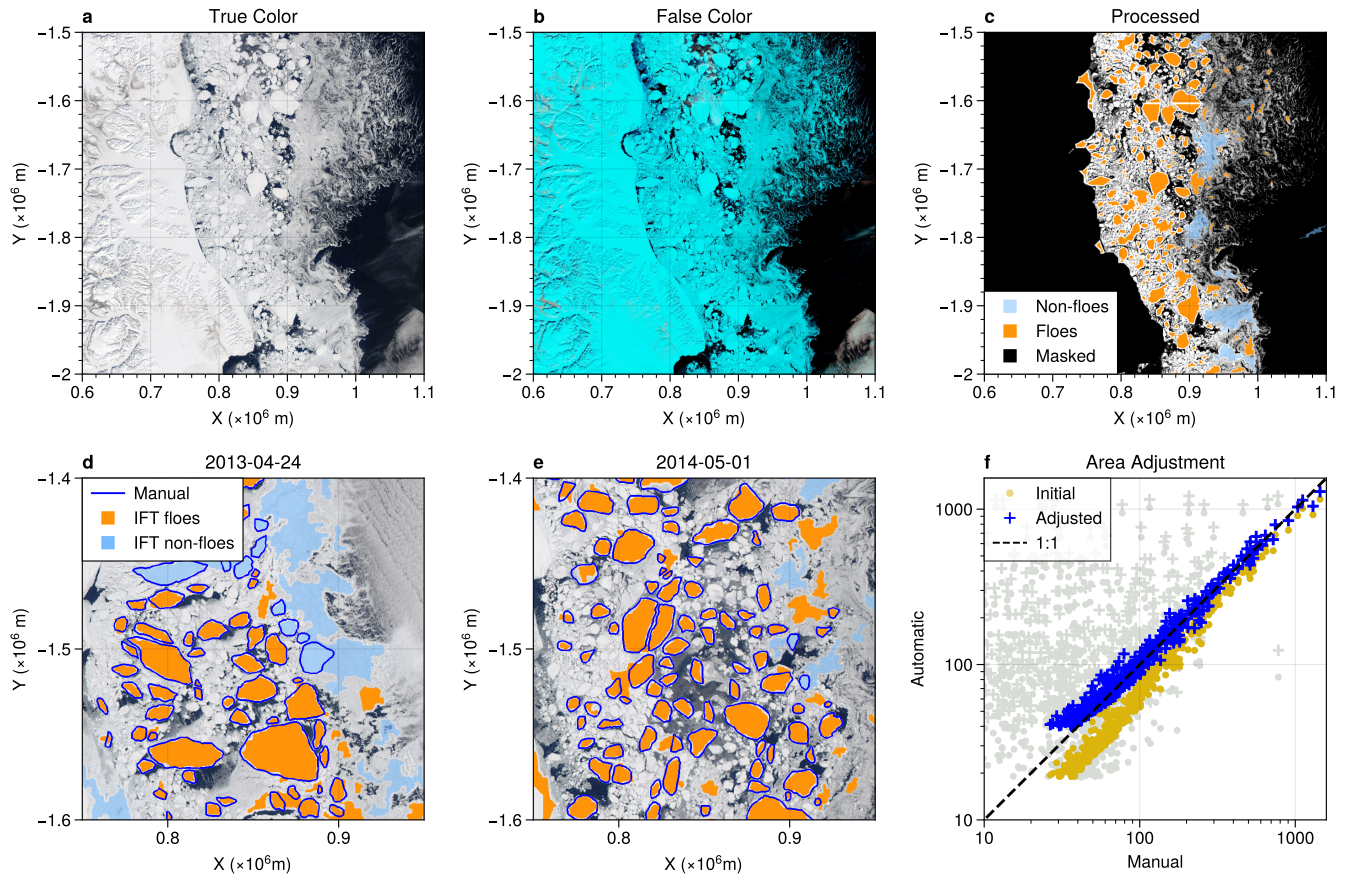


**Fig. 2.** Top: True color (a), false color (b), and processed (c) images for 2014-05-01 from the *Aqua* satellite. In the processed image, masked regions (including the dilated land mask and the cloud mask) are black. Candidate segments are labeled as either floes (orange) or non-floes (light blue); non-floes are discarded in the final product. Bottom: Details of *Aqua* true color images from (d) 2013-04-24 and (e) 2014-05-01 with overlaid IFT segmentation results, with objects labeled as floes marked in orange and discarded objects in light blue. Manually identified floe boundary for the true positive floes are shown in dark blue. Panel (f) shows the area of manually labeled well-segmented objects versus IFT results for the dates shown in (d) and (e) initially (gold) and after area adjustment (blue). Objects with poor correspondence to manual floe labels are marked in gray. The one-to-one line is shown in black. Image locations are shown in Fig. 1.

154 *Gridded sea ice data products*

155 We use the NSIDC Daily Ice Motion Vectors data product of time-average sea ice drift at moderate to  
 156 large scales (Tschudi and others, 2020). This product merges ice motion estimates from passive microwave  
 157 imagery, buoys, and from reanalysis wind data. The motion vectors are provided on a 25-km grid at daily  
 158 resolution. Note, however, that the effective resolution is generally coarser than this, as the source satellite

159 motion resolution is 37.5-75 km (Tschudi and others, 2020). We use sea ice concentration (SIC) from  
160 the NOAA/NSIDC Climate Data Record (CDR) of Sea Ice Concentration. This product combines SIC  
161 estimates from the NASA Team and NASA Bootstrap algorithms by choosing the maximum concentration  
162 from each (Meier and others, 2021, 2022). We estimate local sea ice concentration at floe positions via  
163 nearest-neighbor interpolation. We calculate the distance to the ice edge by finding the minimum distance  
164 between each floe and the set of pixels with zero concentration in the SIC CDR. Similarly, we estimate the  
165 distance to the coast by searching for the minimum distance to the grid cells in the NSIDC data products  
166 flagged as land.

167 *Ice Floe Tracker algorithm*

168 The IFT algorithm identifies and tracks ice floe shapes in an image sequence to reconstruct their motion  
169 trajectories. The algorithm consists of five subroutines: (1) image acquisition, (2) pre-processing, (3)  
170 feature extraction, (4) floe tracking, and (5) data post-processing. Steps 2-4 are described in detail in  
171 Lopez-Acosta and others (2019); Lopez-Acosta (2021) and are briefly summarized here.

172 Image pre-processing comprises de-noising via anisotropic diffusion filtering, contrast adjustment by  
173 adaptive histogram equalization and unsharp masking, and noise removal by morphological reconstruc-  
174 tion. These procedures produce a sharpened grayscale image (Fig 2c). Next, we apply a combination of  
175 morphological operations and  $k$ -means clustering to segment the pre-processed image into ice and water  
176 regions. Watershed segmentation is applied both to the sharpened image and to the segmented image, then  
177 these watershed outputs are compared to determine a final segmentation. Finally, we label the connected  
178 components of the segmented image and extract shape properties (e.g., area, perimeter, centroid) from  
179 potential floes. The error in discrete representations of shapes tends to increase as the size decreases. In  
180 addition, prior studies have found few floes larger than 30-50 km (Stern and others, 2018a,b). Hence, only  
181 candidate floes with area of at least 300 pixels and at most 90,000 pixels (18.75-5,625 km<sup>2</sup>; length scales  
182 4.3-75 km) are retained.

183 The floe tracking component links floe shapes across image pairs (Fig. 3). For each floe, candidate  
184 matches in subsequent images are selected by first filtering by travel distance and floe area. Potential floe  
185 matches are rotated until the area difference is minimized. If the area difference is sufficiently small after  
186 rotation,  $\psi - s$  curves (Kwok and others, 1990) are calculated for each floe. These curves summarize the  
187 tangent angle,  $\psi$ , and arc length,  $s$ , of each floe. If the  $\psi - s$  correlation is higher than 0.7, the floes are

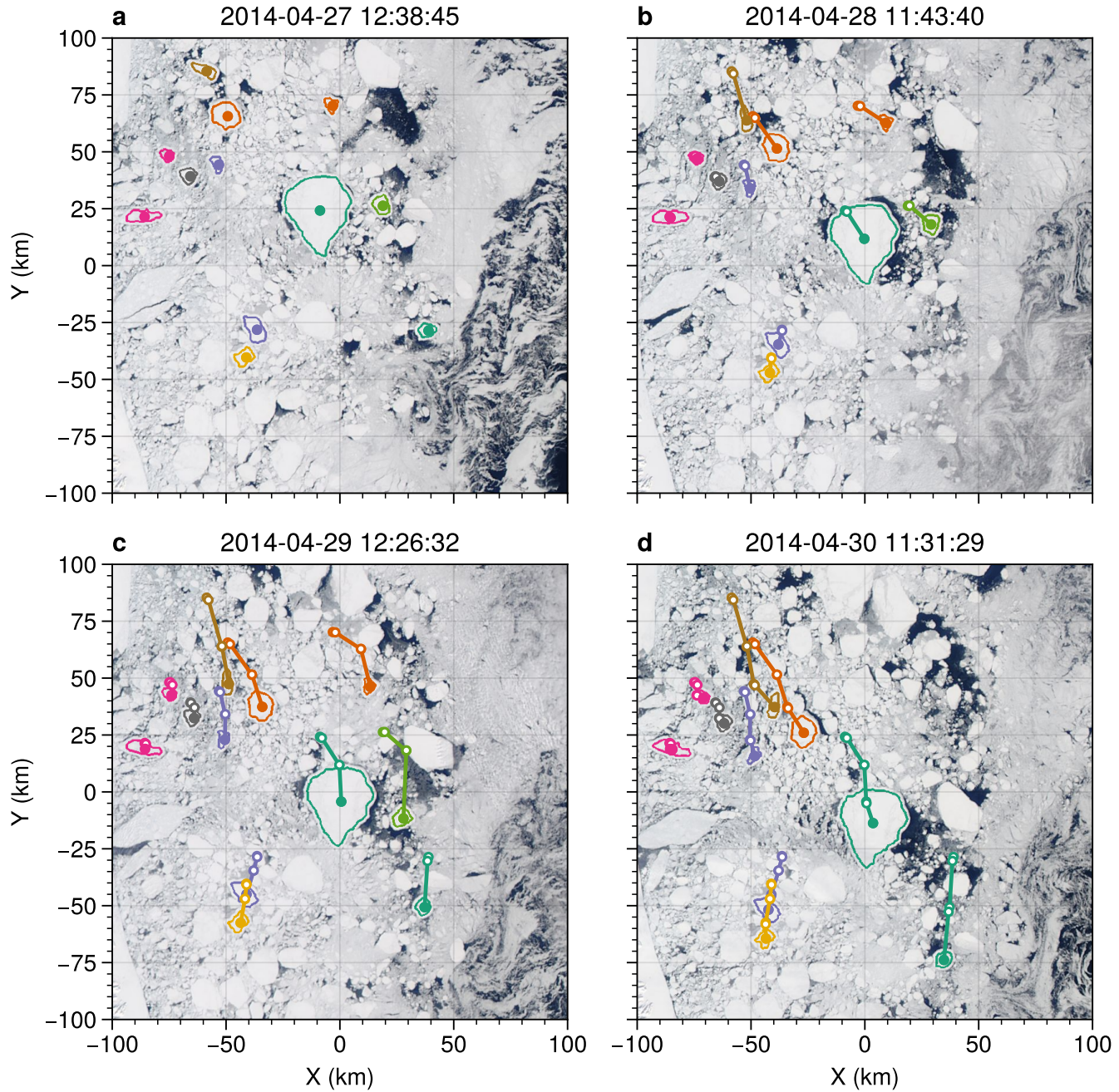


**Fig. 3.** Floe shapes and trajectories for a set of floes tracked in *Aqua* imagery from April 27–30, 2014. Satellite overpass time is marked in the title. Image location is shown in Fig. 1. Markers show the position of the floe centroid at the image time, while hollow circles show the position of the centroid in the previous images.

linked. Whether a floe can be tracked depends mainly on cloud cover, whether the floe remains intact, and on the algorithm accuracy in identifying the floe shape.

Daily rotation rates are calculated separately for both the *Aqua* and *Terra* satellite images. We use

191 the mean daily rotation across the two satellites when both are available, otherwise we use rotation from  
 192 a single satellite. Rotation rates are then normalized to radians per day. Floe positions are regredded to  
 193 local noon, which is typically less than 2 hours away from the two satellite overpass times.

194 Sea ice motion in the IFT is derived from matched pairs of ice floes across multiple days. Thus, as is  
 195 the case for other remote sensing-based ice drift estimates, we can only measure net displacement between  
 196 acquisition times, rather than measuring the instantaneous floe velocity. The mean floe speed during a day  
 197 is bounded below by the net displacement per day. Ice motion vectors

$$198 \quad \mathbf{u}_{IFT} = (u_{IFT}, v_{IFT}) \quad (2)$$

199 are estimated from the floe centroid time series with reference to the polar stereographic projection. Up  
 200 to two position estimates are available for each day corresponding to the *Aqua* and *Terra* overpass times.  
 201 We regrid the centroid positions to a fixed-time grid using bilinear interpolation, and estimate the motion  
 202 using forward differences.

### 203 Post-processing

204 The IFT image processing returns significantly more candidate ice floe shapes than it is able to track.  
 205 These candidate ice floe shapes contain both untracked floes and false positives, such as ice filaments and  
 206 clouds. In Lopez-Acosta and others (2019), the floe tracking served as a filter to remove objects such as  
 207 bright clouds that had been mislabeled as sea ice. In order to leverage shapes from untracked floes for  
 208 FSD analysis, we developed a post-processing routine to identify which of the untracked objects are likely  
 209 to be ice floes. The light blue regions in Fig. 2d and e are examples of rejected shapes. We implemented  
 210 a logistic regression classifier to assign each object a probability of being an ice floe. Training and testing  
 211 the classifier required identifying a set of true and false positives. True positives were selected from the  
 212 set of tracked floes such that (a) trajectory mean drift speeds are less than than 1 m/s and (b) trajectory  
 213 maximum drift speed is larger than 0.05 m/s, i.e., moving at least two pixels per day. False positives were  
 214 identified using circularity and solidity thresholds. Circularity is defined as

$$215 \quad C = \frac{4\pi A}{P^2} \quad (3)$$

216 where  $A$  is the floe area and  $P$  is the floe perimeter, such that a perfect circle has  $C = 1$ , while solidity  
 217  $S$  is the ratio of the area of the shape to the area of the smallest enclosing convex polygon. Objects with  
 218  $S \leq 0.4$  or  $C \leq 0.2$  were labeled as false positives.

219 A final source of false positives comes from estimating the local SIC. We applied nearest neighbor  
 220 interpolation to the NSIDC SIC data to find the sea ice concentration in the nearest grid cell to the IFT  
 221 floe positions. Objects with SIC=0 were classified as false positives. Prior to model fitting, we stratified  
 222 the sample by year and month, randomly selecting up to 1,000 true and false positives from each subgroup.  
 223 The randomly sampled data were split into training and testing portions, then trained using 10-fold cross  
 224 validation. Model fitting was carried out using the Python Scikit-Learn machine learning library (Pedregosa  
 225 and others, 2011). The algorithm performs well, with a precision score of 0.92 and recall score of 0.9.

226 Comparison of the IFT floe shapes with manually annotated imagery shows that the methods used  
 227 to separate neighboring floes produces a systematic underestimate of floe area (Fig. 2d-f). The detected  
 228 floe boundary is an approximately constant number of pixels inside the true floe boundary. As a result,  
 229 the relative error in area is greater for small floes than for large floes. For a floe with detected segment  
 230 area  $A_0$ , we implement a simple bias correction factor by adding a fixed offset  $\delta L$  to the floe length scale  
 231  $L_0 = \sqrt{A_0}$ , such that the corrected area  $A$  is given by

$$232 \quad A(L_0) = (L_0 + \delta L)^2 \quad (4)$$

233 and the corrected length scale is  $L = L_0 + \delta L$ .

234 To find an optimal value for  $\delta L$ , we manually labeled  $n = 1,071$  true floe boundaries for IFT candidate  
 235 floes across five images. Pairs of true floes and candidate floes were divided into test and training sets,  
 236 with 2/3 going into the training set. We then identified quality candidate objects using the area fraction  
 237 of the overlap. Setting thresholds of overlap area to at least 90% of the candidate floe area and 40% of the  
 238 ground truth floe area removed under-segmented objects well, yielding  $n = 440$  well-segmented floe pairs.  
 239 Minimizing the mean absolute error in area using the well-segmented pairs yields an optimal correction  
 240 factor of  $\delta L = 8$  pixels, with a mean absolute error of  $10.6 \text{ km}^2$  (median  $4.9 \text{ km}^2$ ) for the well-segmented  
 241 pairs. Finally, using all test-set floe pairs marked as clean by the logistic regression, absolute error has a  
 242 long tail with a few large outliers, resulting in mean absolute error of  $79.6 \text{ km}^2$  (median  $12.0 \text{ km}^2$ ).

243 *IFT data summary*

244 Detected sea ice floes cover the region of the Greenland Sea where sea ice is typically found. The lowest  
245 detection frequency is near the edge of the seasonal maximum ice extent, and the highest floe concentrations  
246 are seen nearer to the center of the ice tongue (Fig. 4a-b). The highest concentration of detected floes is in  
247 the southern portion of the study area. Trajectories reflect the southward, nonlinear motion of sea ice (Fig.  
248 4c). The raw segmented imagery contain approximately  $10^5$  objects per year, with about half as many  
249 passing the quality control algorithm (blue and orange lines in Fig. 4d). The number of detected floes  
250 passing quality control shows a distinct climatology (Fig. 4e) with many more floes available early in the  
251 year. The number peaks in April and has a secondary peak in June, possibly related to landfast ice breakup.  
252 By July, ice extent is much lower and few images have more than 100 floes. Detecting rotation and drift  
253 requires pairs of images and successful floe matching, resulting in the number of rotation estimates being  
254 on the order of  $10^3$  per year; since an individual trajectory can have multiple rotation measurements, the  
255 number of individual tracked objects is slightly reduced (pink and green lines in Fig. 4d). Most trajectories  
256 are between two and ten days long, and the number of trajectories has strong inter-annual variability (Fig.  
257 4f).

258 **METHODS**259 **Floe size distribution**

260 The sea ice FSD has been shown to be approximately linear in log-log space for at least some range of floe  
261 sizes. As such, it has frequently been summarized through fitting a power law of the form in Equation  
262 1 (Rothrock and Thorndike, 1984; Stern and others, 2018b). A common approach to estimating power  
263 law fits of this form from empirical data is to apply a log-transform to the data and fit a line using least  
264 squares. Due to the effects of sparse but high-impact fluctuations in the tail of the distribution, this  
265 method can be inaccurate; furthermore, the least squares method does not test whether a power law is  
266 appropriate (Clauset and others, 2009; Bauke, 2007; Goldstein and others, 2004). Other distributions,  
267 such as a truncated power law or lognormal distribution, may fit the data better, while still explaining  
268 the approximately linear scaling seen in the log-log plots (e.g., Toyota and others, 2006; Herman, 2010;  
269 Burroughs and Tebbens, 2001; Montiel and Mokus, 2022; Lu and others, 2008). In this study, we follow  
270 the approach of Clauset and others (2009), as implemented in the Python `powerlaw` package (Alstott and

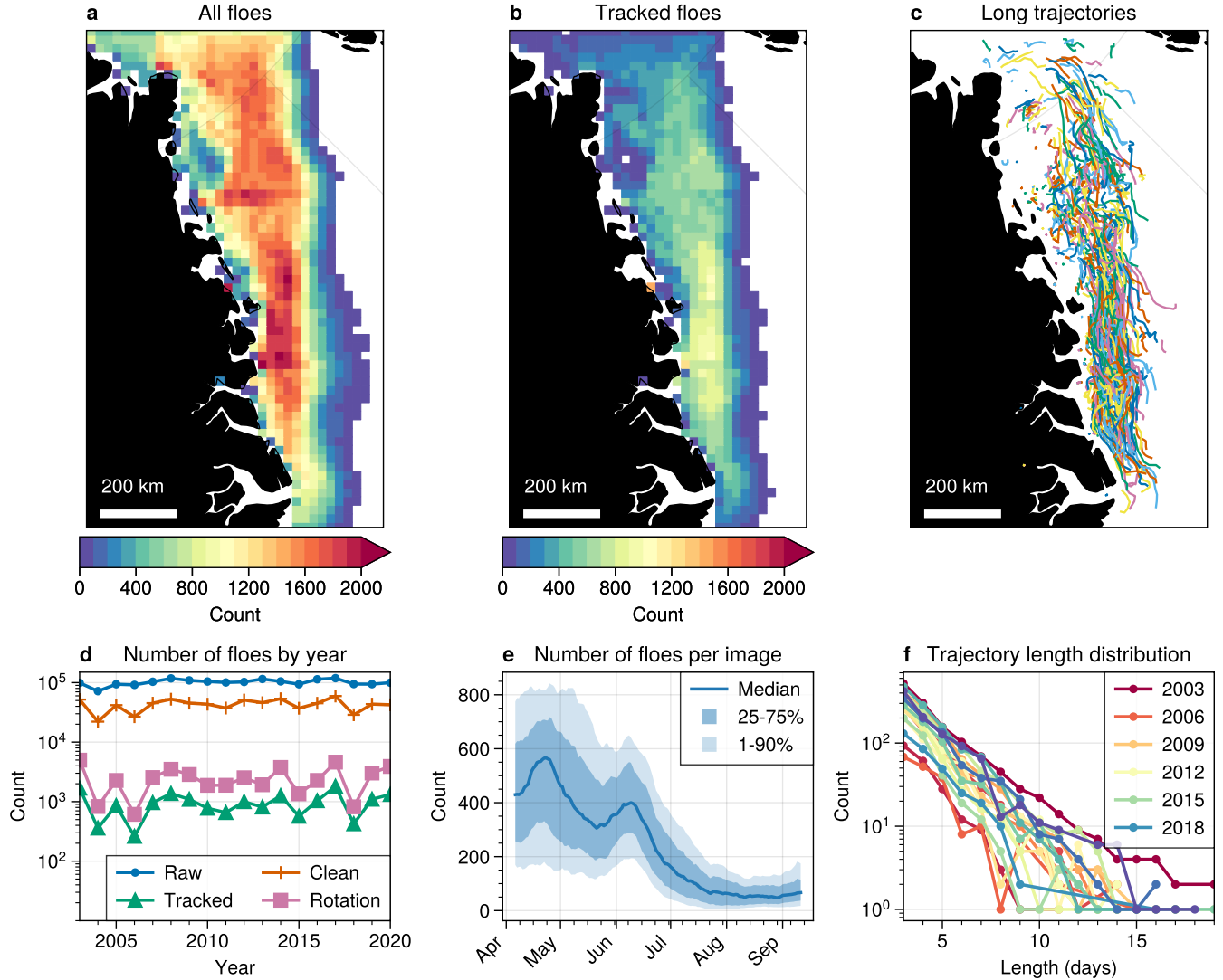


**Fig. 4.** Top: spatial histograms of (a) all available sea ice floe shapes and (b) tracked floes. Floe centroids were binned into 25 km by 25 km grid cells for enumeration. (c) Ice floe trajectories for floes tracked for a period of at least 7 days. Bottom: (d) Number of floes per year in the raw IFT output (blue) and after postprocessing (orange). The number of tracked floes is shown in green and the number of rotation rate estimates is in pink. (e) Distribution of the number of floes per image as a function of day of year. Counts were smoothed using a 15-day centered median. (f) Histograms of trajectory lengths in days for each year.

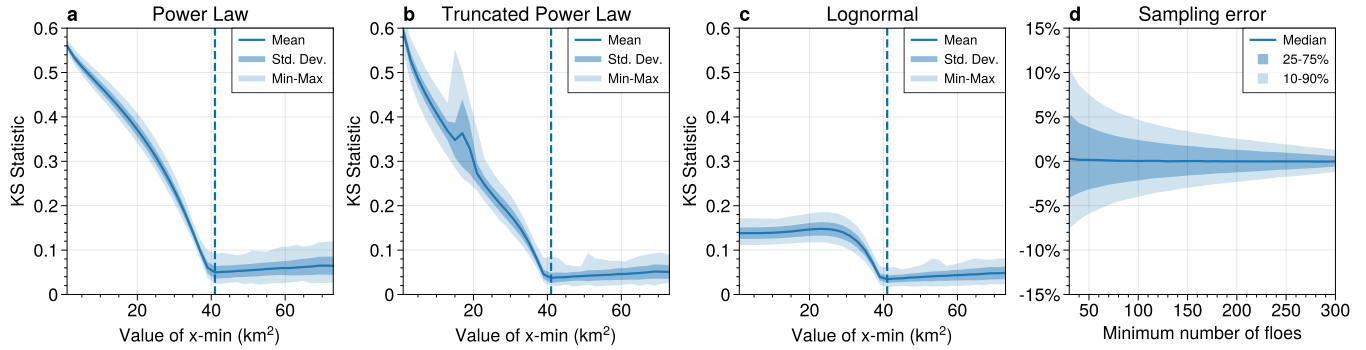


**Fig. 5.** Ensemble mean (solid line), standard deviation (dark shading), and min-max range (light shading) of  $D_{KS}$  for the best-fit parametric distribution as a function of  $x_{min}$  for (a) power law, (b) truncated power law, and (c) lognormal distributions. Vertical dashed lines mark  $x_{min} = 41 \text{ km}^2$ . (d) Relative error in power law  $\alpha$  estimate by subsample size relative to images with greater than 300 floes. Shading as in (a-c).

others, 2014). We focus on the power law, truncated power law, and lognormal distributions due to their frequent use in the literature. Multiple distributions are referred to as truncated power laws across different studies. Here, we use the form

$$p(x) = cx^{-\alpha}e^{-\lambda x} \quad (5)$$

where  $p(x)$  is the probability of a floe having area  $x$ ,  $c$  is a normalizing constant,  $\alpha$  is the power law slope parameter, and  $\lambda$  is a parameter controlling the rate of cut-off as  $x$  grows large. The lognormal distribution is defined using parameters  $\mu$  and  $\sigma$  and has the probability density function (PDF)

$$p(x) = \frac{1}{x\sigma\sqrt{2\pi}} \exp\left(-\frac{(\ln x - \mu)^2}{2\sigma^2}\right). \quad (6)$$

Best-fit parameters for each distribution are identified using maximum likelihood.

Since the fitted distribution depends on the minimum value of  $x$ , we apply a constant  $x_{min}$  for the full analysis. The optimal  $x_{min}$  is determined by a simple numerical experiment. Using 300 randomly selected images, for each value of  $x_{min}$  from 1 to 75  $\text{km}^2$  we find the best-fit parameters for each parametric distribution. The Kolmogorov-Smirnov distance  $D_{KS}$ , defined as the supremum of the distance between the data and the best fit parametric distribution, is used to measure the goodness of fit. The optimal  $x_{min} = 41 \text{ km}^2$  is found by minimizing the ensemble mean  $D_{KS}$  (dashed line in Fig. 5a-c). The model fit improves rapidly as  $x_{min}$  increases to  $41 \text{ km}^2$ , then degrades past that value.

It is important to note that the IFT dataset provides a sample of floes in each image, not a complete

enumeration. The identifiable floes are constrained by the characteristics of MODIS data, including its 250 m spatial resolution and frequent cloud cover that obscures many floes in the visible imagery. Even though the post-processing performs well, some false positives remain in the floe library, adding further uncertainty to the estimated FSD. The MODIS images and the bounds of the study domain are sufficiently large such that the maximum observable floe size is not constrained by image dimensions, meaning finite size effects (Stern and others, 2018b) have a minimal impact on the tail of the recovered distribution. However, our ability to estimate the FSD in a scene based on a sample of floes depends on the sample size. In the absence of large sets of manually annotated imagery, we simulate the effect of subsampling by computing the relative error in power law  $\alpha$  estimates. We randomly selected 100 images with at least 300 floes in each, then repeatedly sampled  $n$  floes from each image without replacement and recalculated  $\alpha$ . We chose the minimum threshold of floes per image for FSD analysis based on a pragmatic balance between the number of floes available in a typical image by day of year (Fig. 4e) and the estimated sampling uncertainty (Fig. 5d). With  $n = 100$ , we have  $\alpha$  errors within  $\pm 5\%$  in 80% of cases, while still retaining some late-summer data.

In addition to the image-by-image calculation, we also calculate FSD fits for the data binned by day of year. This estimates a central tendency of the distribution, and enables us to estimate FSD later in the year when the per-image sample size is too low.

We weigh the suitability of the three candidate parametric distributions for describing the observed FSD. The distance between the fitted and empirical distributions was assessed with the K-S statistic  $D_{KS}$ . P-values are determined by repeatedly drawing samples from the fitted distribution, calculating the fit to the sampled values, and calculating  $D_{KS}$ . The p-value is then determined by the percentage of the K-S statistics from the resampling procedure that are larger than the  $D_{KS}$  for the original data.

### 310 Sea ice drift vector decomposition

311 The sea ice drift vector  $\mathbf{u}$  can be decomposed into an along-track (longitudinal) component  $\mathbf{u}_L$  and a  
 312 cross-track (transverse) component  $\mathbf{u}_T$  as:

$$313 \quad \mathbf{u} = \mathbf{u}_L + \mathbf{u}_T. \quad (7)$$

314 The longitudinal and transverse perturbations  $\mathbf{u}'_L$  and  $\mathbf{u}'_T$  are computed by subtracting the mean flow from  
 315 the instantaneous floe drift vectors, and then calculating the longitudinal and transverse components of

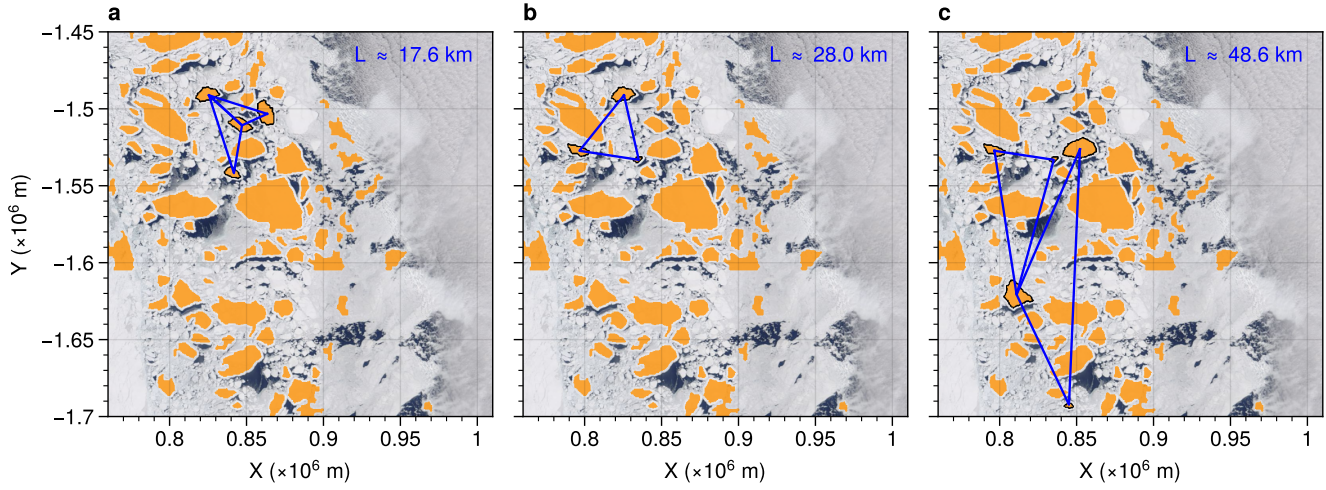


**Fig. 6.** Detected floe shapes in the Terra image for April 24, 2013 (orange). Triangles formed using selected ice floes as vertices (outlined in black) are used to calculate area-averaged strain rates. Examples of triangles at length scales of (a) 17.6 km, (b) 28 km, and (c), 48.6 km length scales are shown, with the length scale defined as the square root of the triangle area.

316 the drift anomalies. The transverse drift component is often termed the *perturbation velocity*. Similar to  
 317 Gabrielski and others (2015), we use centered-time averages of the NSIDC Ice Motion Vectors product to  
 318 represent the mean flow, however here, we are also examining the anomalies relative to the mean flow.  
 319 Note that properties of  $\mathbf{u}_T$  likely depend on the choice of the mean flow  $\langle \mathbf{u} \rangle_\tau$ , where  $\tau$  is the averaging  
 320 time scale (e.g., Rampal and others (2009)); here, we consider the effects of different time-average windows  
 321  $\tau \in (5, 10, 15)$  where  $\tau$  is time in days.

### 322 Strain rate estimation

323 Area-averaged strain rates are calculated using Green's theorem from sets of point estimates of sea ice  
 324 velocities along a polygon boundary (e.g. Kwok and others (2003); Hutchings and others (2012); Rampal  
 325 and others (2019); Dierking and others (2020)). Given a set of  $N$  ice floe positions  $x$  and motion estimates  
 326  $\mathbf{u}(x)$ , we iterate over all possible triangles formed by subsets of floe positions and retain all triangles with  
 327 minimum interior angle of  $20^\circ$  or greater. This procedure yields millions of polygons; since the number of  
 328 available polygons is bounded above by a combinatorial function, the number of polygons varies widely per  
 329 year. Using all possible polygons, as was done in Itkin and others (2017), results in considerable overlap  
 330 between polygons in some regions. Due to the large study area, we find that the degree of polygon overlap  
 331 varies considerably from small to large scales, which may lead to uneven spatial weighting across scales.

332 Small polygons are generally non-overlapping, and large polygons nearly all overlap. To minimize spatial  
 333 biases from overlapping polygons, we downsample iteratively to find sets of non-overlapping polygons  
 334 within logarithmically-spaced length scale bins. In each image, we randomly choose a starting polygon,  
 335 then iterate through the list of remaining polygons, keeping a polygon if the intersection with previously  
 336 chosen polygons has zero area (e.g., Fig. 6). For consideration of spatial scaling, we further downsample  
 337 by drawing random samples within each length scale bin so that equal numbers of samples within each bin  
 338 are used.

339 The Green's theorem approach for strain rate calculation uses the line integral around a region to  
 340 calculate the area average of the gradient of a quantity. Given drift vectors  $\mathbf{u} = (u, v)$  measured at  $N$   
 341 points  $\mathbf{x} = (x, y)$  forming the vertices of a polygon, the mean velocity gradients within the polygon are  
 342 calculated as

$$\begin{aligned} 343 \quad \bar{u}_x &= \frac{1}{A} \oint u \, dy \\ 344 \quad &\approx \frac{1}{2A} \sum_{i=1}^N [(u_{i+1} + u_i)(y_{i+1} - y_i)], \end{aligned} \quad (8)$$

346 where in the summation notation used here, the calculation wraps clockwise around the polygon to the  
 347 origin. Hence, for the triangles used here,  $x_4 = x_1$ . Other ice drift gradients are calculated in a similar  
 348 fashion (see e.g. Lindsay and Stern (2003); Hutchings and others (2018); Bouchat and Tremblay (2020)  
 349 for details.)

350 From these spatial gradients we calculate the invariants of the strain rate tensor  $\dot{\varepsilon}$  (Leppäranta, 2011):

$$351 \quad \dot{\varepsilon}_I = \bar{u}_x + \bar{v}_y \quad (9)$$

$$352 \quad \dot{\varepsilon}_{II} = \sqrt{(\bar{u}_x - \bar{v}_y)^2 + (\bar{u}_y + \bar{v}_x)^2} \quad (10)$$

354 from which we compute the total deformation

$$355 \quad D = |\dot{\varepsilon}| = \sqrt{\dot{\varepsilon}_I^2 + \frac{1}{2}\dot{\varepsilon}_{II}^2}. \quad (11)$$

357 Uncertainty in the strain rate calculations depends on the uncertainty in position  $\sigma_x$  and area  $\sigma_A$ , and on  
 358 the velocities (Dierking and others, 2020). Triangle area uncertainty depends on the side lengths, so for a

359 triangle with sides  $a, b, c$ , the uncertainty in area  $\delta_A$  is given by

$$360 \quad \delta_A^2 = \frac{\delta^2}{4}(a^2 + b^2 + c^2) \quad (12)$$

361 and following Hutchings and others (2012), relative uncertainty in a strain rate component  $\epsilon$  is given by

$$362 \quad \frac{\delta_\epsilon}{\epsilon} = 2 \left( 4 \frac{\delta_x^2}{A} + 2 \frac{\delta_x^2}{U^2 T^2} + \frac{\delta_T^2}{T^2} + \frac{\delta_A^2}{A^2} \right)^{1/2} \quad (13)$$

363 From Lopez-Acosta and others (2019), the position error for ice floes detected by the IFT is comparable  
 364 to the resolution of the MODIS imagery, so  $\delta_x \approx 255$  m, and ice drift error  $\approx 0.65$  cm/s. We considered  
 365 the effects of minimum interior angle on the strain rate uncertainty by calculating the uncertainty for a  
 366 right triangle across a range of length scales. Based on this analysis we conservatively choose a minimum  
 367 angle of 20. Uncertainty decreases with increasing length scale: relative area uncertainty is less than 5%  
 368 for triangles with length scale  $L = \sqrt{A_{\text{triangle}}}$  larger than 10 km. Uncertainty in the strain rate decreases  
 369 with increasing triangle area, drift speed, and with decreasing uncertainty in time and space. With  $\delta_T = 1$   
 370 hr,  $\delta_x = 255$  m, and length scale 15 km, relative error  $\delta_\epsilon/\epsilon$  is less than 1 if the drift speed is at least 1  
 371 cm/s, and less than 0.2 if the drift speed is at least 5 cm/s. For the scale analysis, we discard polygons  
 372 with relative uncertainty greater than 0.5. Mean relative error for the analyzed length scales decreases  
 373 monotonically from 0.16 (bin 1, mean  $L = 18$  km) to 0.02 (bin 5, mean  $L = 67$  km).

### 374 Length scale parameter estimation

375 The length scale dependence of deformation is estimated as

$$376 \quad D \sim L^{-\beta}, \quad (14)$$

377 where  $L$  is the length scale of the observation; here, we use  $L = \sqrt{A_{\text{triangle}}}$ . Numerous methods have  
 378 been used to estimate the strain rate scaling parameter  $\beta$ . For example, Marsan and others (2004) and  
 379 Hutchings and others (2011) fit a regression line to the logarithm of the bin-averaged total deformation,  
 380 while Itkin and others (2017) fits the regression function using the full set of log-transformed points.

382 We analyze the scale dependence using both the standard bin-averaging approach, and introducing a  
 383 new approach in which the parameter  $\beta$  is treated as an unknown parameter for the distribution of the

384 scaled total deformation. The new approach uses a stratified sample across all length scale bins, rather  
 385 than fitting to a small number of bin averages. Formally, we hypothesize that the scaled total deformation

$$386 \quad D^*(\beta) = D/L^{-\beta} = DL^\beta \quad (15)$$

387 is lognormally distributed. Lognormal distributions arise from the central limit theorem when independent  
 388 positive random variables are combined multiplicatively rather than additively. Lognormal distributions  
 389 are observed in the plastic deformation of numerous materials (Tang and others, 2020; Chen and Korsunsky,  
 390 2021) and have been discussed previously in the context of sea ice deformation (Marsan and others, 2004).  
 391 Under this assumption, the logarithm of the scaled total deformation is normally distributed

$$392 \quad \log D^* \sim \mathcal{N}(\mu, \sigma^2) \quad (16)$$

393 with parameters  $\mu$  and  $\sigma^2$  dependent on the parameter  $\beta$  and data  $D_i^*$  such that

$$394 \quad \mu(\beta) = \frac{1}{N} \sum_{i=1}^N \log D_i^*(\beta) \quad (17)$$

$$395 \quad \sigma^2(\beta) = \frac{1}{N} \sum_{i=1}^N [\log D_i^*(\beta) - \mu(\beta)]^2 \quad (18)$$

397 where  $N$  is the total number of triangles and  $D_i^*$  is the scaled total deformation of the  $i$ th triangle. While  
 398 these are, of course, the standard maximum likelihood estimates for the parameters of a normal distribution,  
 399 at this stage the  $\beta$  parameter needed to calculate  $D^*$  is unknown. Our approach is to numerically find the  
 400 maximum of the log likelihood function for  $\mathcal{N}(\mu, \sigma)$ . The log likelihood function given  $N$  observations of  
 401 deformation  $D_i^*$  and length scale  $L_i$  is

$$402 \quad \log \mathcal{L}(\beta | D, L) = -\frac{N}{2} \log(2\pi\sigma^2(\beta)) \\ 403 \quad - \frac{1}{2\sigma^2(\beta)} \sum_{i=1}^N [D_i^* - \mu(\beta)]^2 \quad (19)$$

404 The parameter  $\beta$  is then estimated numerically by maximizing  $\log \mathcal{L}(\beta | D, L)$  over  $\beta \in (0, 1]$  using a  
 405 stratified random sample of non-overlapping polygons from logarithmically-spaced length-scale bins. We  
 406 calculate a bootstrap confidence interval for  $\beta$  using the quantile method with 1,000 bootstrap replicates.  
 407 The performance of the lognormal log-likelihood approach for estimating the total deformation scaling pa-

409 parameter is evaluated by comparison with the empirical distributions within length scale bins and comparison  
410 with the regression-based methods from the literature.

## 411 Simulations

412 We examine the effects of mesoscale and submesoscale oceanic eddies on ice motion using a discrete element  
413 sea ice model (SubZero, Manucharyan and Montemuro (2022)), coupled with a two-layer quasi-geostrophic  
414 (QG) ocean model (Arbic and others, 2012). The main adjustable parameters in the QG model are the  
415 bulk vertical shear  $\Delta U$ , the Rossby deformation radius  $R_d$ , and the top/bottom ocean layer depth ratio  
416  $\delta$ . We apply the parameter values  $\Delta U = 0.21$  m/s,  $R_d = 5.2$  km and  $\delta = 1$  developed in a prior analysis  
417 of floe motion in the Beaufort Sea (Manucharyan and others, 2022). These values produced the optimal  
418 model performance against a loss function based on a comparison of IFT-observed and simulated ice floe  
419 rotation rate variances for isolated ice floes in the Beaufort Sea. To tune the model, we change the model  
420 parameters to generate different ocean flow fields in which floes are advected and rotated. The loss function  
421 was defined as the difference between simulated and observed rotation rate variances, normalized by the  
422 observed variance. The tuning started with  $\Delta U = 0.30$  m/s,  $R_d = 13$  km and  $\delta = 0.1$ , and was iteratively  
423 adjusted to the final values, resulting in a loss function value of 0.19. After tuning, the ocean flow fields are  
424 initialized with these best-fit values and allowed to equilibrate over a simulated year to ensure a converged  
425 kinetic energy spectrum. Simulations use a square 400 km  $\times$  400 km periodic domain with 256 Fourier  
426 modes.

427 The surface velocities from the QG model are then used to drive the translation and rotation of ice  
428 floes with the SubZero model. Ice floes in the model are represented as circular rigid bodies with constant  
429 thickness (0.5 m) and are subjected to ocean stresses, the Coriolis force, and pressure gradient forces  
430 resulting from sea surface height gradients. Here we consider floes with length scales ranging from 1 km to  
431 50 km. The forces and torques acting on each floe are spatially integrated over their area at each time step  
432 using a Monte-Carlo scheme (Caflisch, 1998). Wind forcing and floe-floe contact are neglected to focus on  
433 quantifying the contribution of oceanic forcing to ice floe motion. Observed ice thickness in the Fram Strait  
434 is highly variable, with values around 0.5 m being more typical of the southern end of the domain than the  
435 northern end (compare Spreen and others (2020); Brunette and others (2022)). We adopt a constant ice  
436 floe thickness to simplify the model and reduce variability in ice floe rotation rates resulting from changes  
437 in floe thickness (or inertia). Recent work (Kim and others, 2024) suggests that floe thickness within the

438 observed range has a negligible effect on the kinematic link between ice floe rotation rates and underlying  
439 ocean vorticity, indicating that this rotational relationship can be effectively captured under the current ice  
440 floe configuration. The ocean fields are updated daily in the simulation to match their temporal resolution  
441 with that of the observed sea ice data.

442 For each floe length scale, we randomly place  $n = 4,000$  floes onto the QG ocean flow field and allow  
443 them to be advected by the ocean currents for 30 model days. The results are insensitive to further  
444 refinement of the ocean resolution and to increases in the number of floes. Daily displacements and  
445 rotations are used to calculate ice floe drift and rotation rate for compatibility with the time resolution of  
446 the observations. Drift speed perturbations are evaluated by subtracting the five-day averaged displacement  
447 from the daily displacement.

## 448 RESULTS

### 449 Floe size distribution

450 We analyze FSD variability by examining the estimated power-law slope on an image-by-image basis and  
451 through binning data across multiple images by day of year (DOY-binning). Images with suitable numbers  
452 of sea ice floes for FSD estimation are found primarily in the early part of the season (Fig. 4e). After  
453 mid-July, few images have more than 100 detected floes, so late-summer FSD is only approached with the  
454 DOY-binned data. The decrease in floe numbers over the season is consistent with the known seasonality  
455 of the ice cover. As the melt season progresses, the ice extent decreases, limiting the area where floes can  
456 be found. Furthermore, we expect the size of floes to decrease through the season, as floes fracture and  
457 melt. A temporary increase in floe count starting in mid-May and extending until mid-June is observed,  
458 consistent with the timing of landfast ice breakup in the Greenland Sea (Wadhams, 1981; Walsh and others,  
459 2022).

460 We next consider the choice of parametric distribution for summarizing the FSD. At a significance  
461 level of 5%, we find that the best fit power-law distribution can be rejected in 23% of the image-by-image  
462 results, which is similar to the results of Hwang and others (2017). When binned by day of year, however,  
463 the power-law fit can be rejected in 76% of cases. Stern and others (2018a) evaluated the performance of  
464 the power law for FSD analysis for the Beaufort Sea using the same goodness-of fit test, and found better  
465 agreement with the standard power law form than we find here. This may be due to regional differences, or  
466 to a difference in methodology—their work uses the mean caliper distance rather than the area to describe

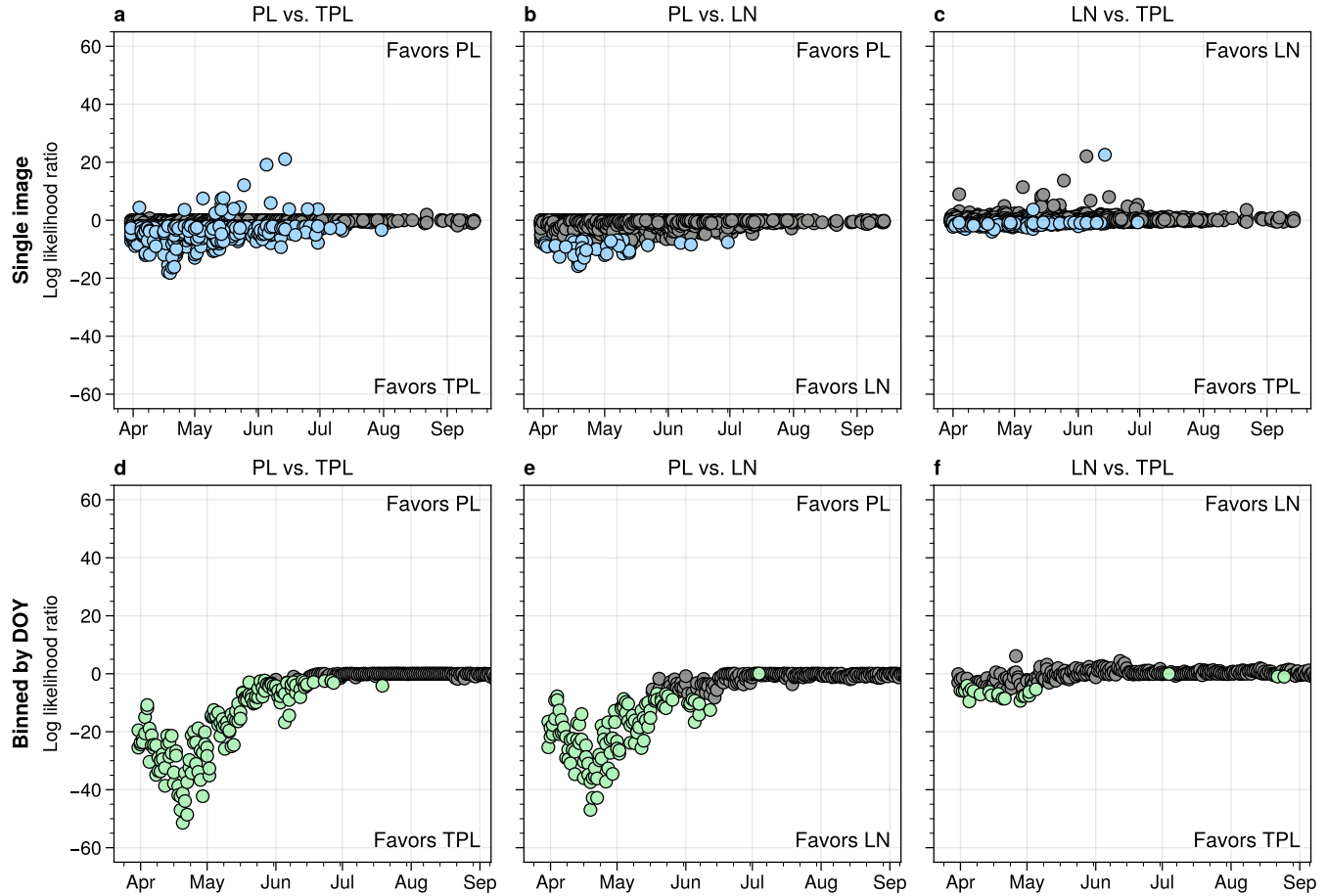


**Fig. 7.** Log-likelihood ratios for image-by-image (top row) and DOY-binned (bottom row) FSD parametric distribution fits. In the figure titles, PL=power law, TPL=truncated power law, and LN=lognormal. Log likelihood ratios that are significantly different than zero after accounting for the false discovery rate are colored blue (image-by-image) or green (DOY-binned). Gray dots are not significantly different than zero. Positive values favor the distribution listed first, and negative values favor the distribution listed second, so for example in panel (a) the negative values favor the truncated power law over the standard power law.

467 variation in floe size.

468 The log-likelihood ratio results show that the standard power law is either less likely than the truncated  
 469 power law or lognormal distribution, or equally likely: only in a handful of images does the standard power  
 470 law provide a significantly better fit (Fig. 7). Seasonality in the likelihood ratio results suggests a shift in  
 471 the form of the FSD through the year. While the sample sizes tend to be lower near the end of the year,  
 472 consistently large samples from April to June provide confidence that the changes seen during that period  
 473 are statistically robust. Mokus and Montiel (2022) argue that wave-driven breakup leads to a lognormal  
 474 FSD. We find that the lognormal distribution is significantly more likely than a standard power law for

475 the DOY-binned data in early summer, when wave-driven breakup is especially likely to be a contributing  
476 factor. It also tends to be more likely than the power law in the image-by-image data. However, in most  
477 cases, we find that the lognormal and truncated power law distributions are equally likely, with a few  
478 exceptions. After July, the log-likelihood ratio test fails to find any difference in likelihood between the  
479 three candidate distributions. In order to facilitate comparison with prior work, we report results for the  
480 truncated power law distribution in the remainder of the study.

481 Examination of the empirical (estimated from the histogram) and fitted PDFs and complementary  
482 cumulative distribution functions (CCDFs) for individual dates shows that the truncated power law provides  
483 a good fit across most of the data, with larger departures from the fit for very large floes (Fig. 8). Gray  
484 lines in the figure show the year-to-year variation in the distributions, which can be substantial. Binning  
485 by day of year (black lines) provides an estimate of the central tendency of the distribution: although  
486 individual dates may show strong deviations (e.g., Fig. 8d), the binned distributions fall within the range  
487 of year-to-year variations.

488 The slope  $\alpha$  of the truncated power law distribution shows distinct seasonality amidst strong variability  
489 (Fig. 9). For April, May, and June, where there are sufficient images meeting the criteria for the minimum  
490 number of floes, we find that the median  $\alpha$  increases from 1.9 in April to 2.2 in July. The interquartile  
491 ranges and interdecile ranges show little variation between months (interquartile range 0.24-0.25, interdecile  
492 range 0.46-0.52). Estimates of  $\alpha$  based on the DOY-binned data fall within the interquartile range of the  
493 image-by-image results. Binning by day of year enables extension of the analysis into late summer. We  
494 find that  $\alpha$  reaches a maximum near  $\alpha = 2.5$  between July and August, then decreases thereafter. For the  
495 time range studied here, the minimum appears to be in April. The increase in power law slope through  
496 the spring-summer melt season has been previously observed in, e.g., the Beaufort Sea (Hwang and others,  
497 2017; Stern and others, 2018a). The seasonality we observe here agrees well with a previous study in the  
498 Beaufort and Chukchi seas (Buckley and others, 2024), in which MODIS imagery was analyzed with a  
499 different segmentation algorithm and found the running-mean  $\alpha$  to range from 1.74 to 2.0 during summer,  
500 with minimum in April and maximum in August. The timing of the minimum and maximum power law  
501 exponent is remarkably similar to the evolution of the FSD for the Beaufort Sea analyzed in Stern and  
502 others (2018a), despite the methodological differences, with minimum  $\alpha = 1.9$  in April and maximum  
503  $\alpha = 2.8$  in August.

504 The pronounced variability in FSD slope is primarily influenced by the strong spatial variability observed

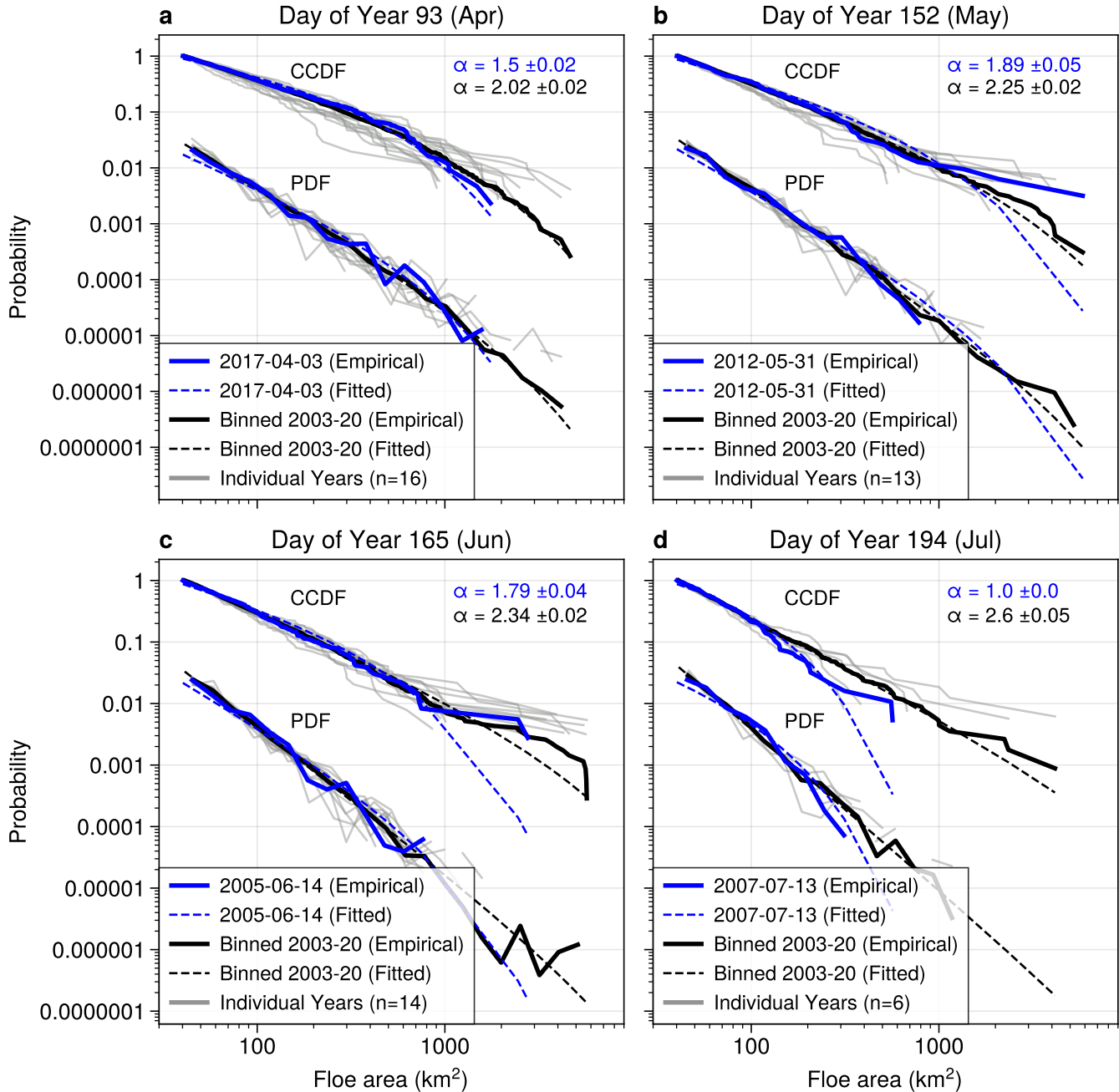


**Fig. 8.** Empirical (solid) and fitted (dashed) FSD PDFs and CCDFs for randomly selected dates in April (a), May (b), June (c), and July (d). Blue lines show the PDF and CCDF for the selected date, gray lines show the distributions for the same day of year for each year with sufficient data, and black lines show the distribution fitted to binned data for the same day of year. Fitted distributions are only shown for the selected date and for the binned data.

505 in the Fram Strait. The position relative the coast line (or fast ice edge) and the position relative to the  
 506 sea ice edge are especially important. Landfast ice on the Greenland coast provides a source of large

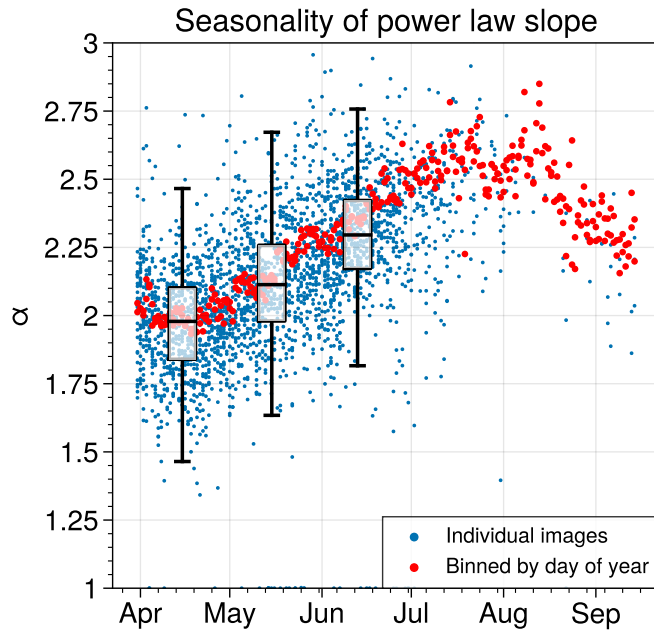


**Fig. 9.** Fitted FSD slope parameter for the truncated power law distribution by day of year for the image-by-image analysis (blue dots) and for the DOY-binned analysis (red dots). Box-and-whisker plots show the interquartile range and median of the image-by-image data for each month.

507 floes as it breaks up through the year. Near the ice edge, wave action increases the likelihood of floe  
 508 fracture, and contact with the relatively warm waters of the North Atlantic enhance local melt rates. Sea  
 509 ice concentration is higher in the north, where ice advected along the Transpolar Drift Stream enters the  
 510 Greenland Sea through the Fram Strait. We examined the dependence of the FSD on SIC and on the  
 511 distance to the ice boundary (coast and open water). While we found some evidence of steeper FSD slopes  
 512 (higher prevalence of small floes) in low-SIC regions and near the coast, detailed examination of the spatial  
 513 variability of FSD slope is beyond the scope of this study.

514 It is worth noting that the analysis thus far has been on the FSD of all detected ice floes, not only the  
 515 ice floes that were successfully tracked. We see that the set of tracked floes tends to have fewer small floes  
 516 and a greater number of large floes relative to the set of all detected floes (Fig. 10). This is unsurprising,  
 517 as larger floes are more likely to have better resolved distinguishing features and shapes than do floes near  
 518 the detection limit. Differences in the distributions in individual years (thin lines) are more extreme than  
 519 the differences across all years. Analysis of interannual variability will need to account for differences in  
 520 the detected floe sizes, however for the remainder of this study, we pool data from multiple years together  
 521 so the results are unlikely to be affected by the differences seen here.

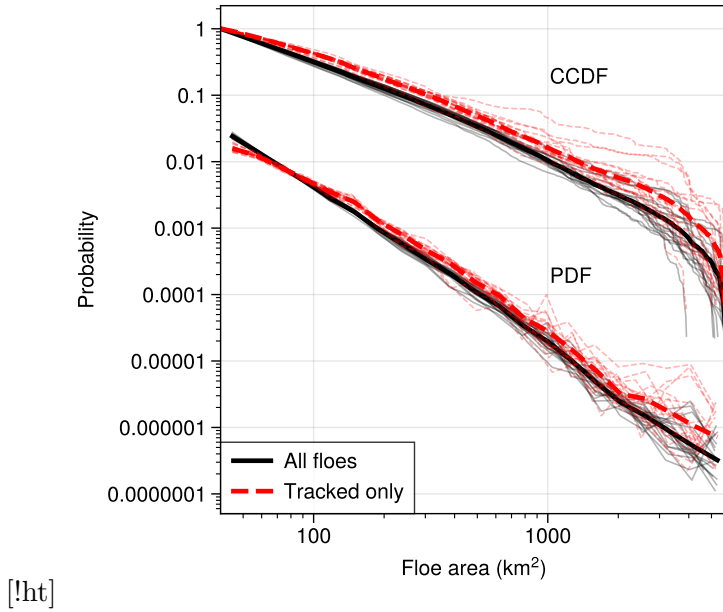


**Fig. 10.** Empirical FSD PDF and CCDF for all floes (solid black line) and for tracked ice floes only (dashed red line). Thick lines show the distribution across all years, while thin lines show the distribution of individual years.

## 522 Sea ice motion

523 We compare the IFT observations to the NSIDC ice motion vectors by binning the observations into 25  
 524 km bins (approximately the maximum spatial resolution of the NSIDC product) and by calculating the  
 525 monthly means across all years (Fig. 11). Means are calculated only for times and locations where both  
 526 IFT and NSIDC data are available. Only bins with at least 30 observations are included in the comparison.  
 527 We find that the direction of the mean drift compares well to the NSIDC mean (Fig. 11a-c). The difference  
 528 between the daily IFT and NSIDC vectors,

$$529 \quad \mathbf{u}' = \mathbf{u}_{IFT} - \mathbf{u}_{NSIDC}, \quad (20)$$

530 is largely distributed along the climatological mean flow. The mean difference shows spatial variability,  
 531 with the largest vector differences occurring in the southern and eastern edges of the ice tongue. Mean  
 532 differences for the months shown are 8.6, 8.9, and 11 cm/s, respectively.

533 Considering the longitudinal and transverse components of the drift vectors, we see larger variance in  
 534 the longitudinal direction than in the transverse direction for both IFT and NSIDC. In both cases, the  
 535 variance for IFT is larger than NSIDC (Fig. 12). Co-variability of the IFT and NSIDC ice drift vector

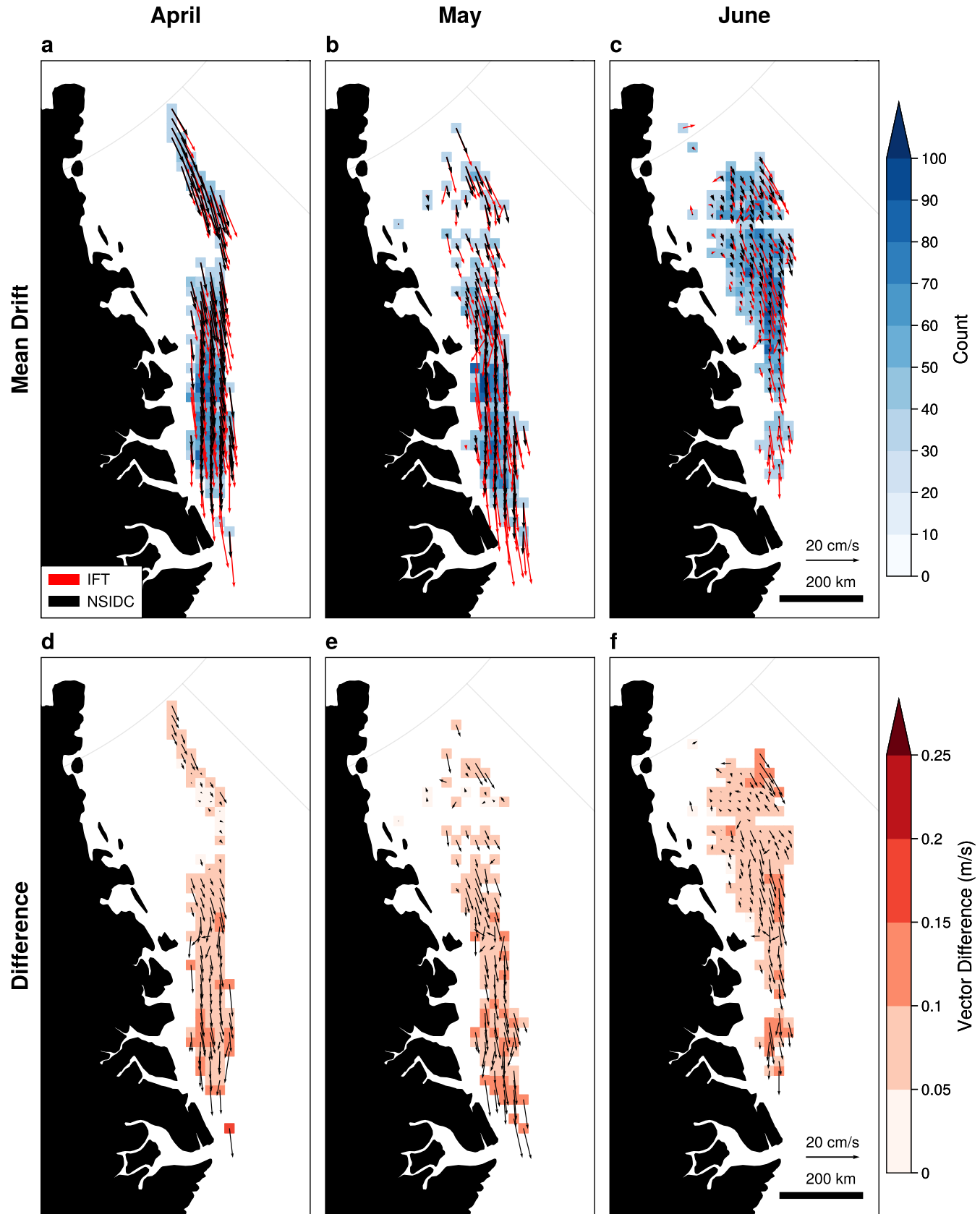


**Fig. 11.** Top: Mean daily drift vector for IFT (red) and NSIDC (black). The length of the vector is proportional to its magnitude. The observation count is shaded in blue. Bottom: Black arrows show the vector difference. The magnitude of the difference is shaded in red.

536 components was measured by Spearman's rank correlation coefficient. Correlation is highest in April  
537 ( $\rho = 0.68$  for longitudinal,  $\rho = 0.7$  for transverse) and lowest in July ( $\rho = 0.13$  for longitudinal,  $\rho = 0.18$   
538 for transverse).

539 For the NSIDC ice motion product, Tschudi and others (2020) noted that the theoretical limit to the  
540 precision of the low-resolution (25 km) passive microwave (PM) derived motion vectors is approximately 7  
541 cm/s, while with the higher resolution PM-derived motion available from AMSR-E produces errors closer  
542 to 5 cm/s (Meier and Dai, 2006). Uncertainty tends to be higher in summer and in the MIZ. Wang and  
543 others (2022) compared the NSIDC data to buoy data in the East Greenland region and found errors of  
544 6.62 km/d (7.7 cm/s). Thus the difference between the NSIDC and IFT ice motion estimates is of similar  
545 size to prior estimates of the NSIDC uncertainty.

546 Uncertainty in gridded motion products arises from numerous sources, including sub-grid-scale ocean  
547 turbulence, which can contribute to velocity variability. In the MIZ, the influence of mesoscale eddies is  
548 strong. The Rossby radius of deformation in the Greenland Sea region is approximately 5 km (Nurser  
549 and Bacon, 2014), and observations of eddies by Kozlov and Atadzhanova (2021) showed mean diameters  
550 of 6-12 km depending on ocean depth. The 25 km-minimum spatial resolution of the NSIDC ice motion  
551 vectors is thus coarse enough that unresolved eddies within a grid cell may have a significant influence on  
552 the uncertainty of grid-mean motion vector.

553 We explore the possibility that ocean eddy activity contributes to the variability of  $\mathbf{u}'$  using the DEM  
554 simulations. If the sub-grid variability were to arise due to ocean eddy activity, then we would expect  
555 that the variability of  $\mathbf{u}'$  would be similar to the variability of ice floes in an idealized eddy-rich ocean  
556 field. Since the distribution of  $\mathbf{u}'$  shows little dependence on the length of the time averaging window  
557 (Fig. 12a, d), we focus on the case with  $\tau = 5$  days. The observed  $\mathbf{u}'$  distribution scaled by the standard  
558 deviation produces a wide-tailed distribution that is very similar to the results of the simulation (Fig.  
559 12b, e)). If  $\mathbf{u}'$  was Gaussian, then the scaled distribution would be equivalent to a normal distribution  
560 with standard deviation 1, shown with a dashed line. In contrast, an exponential distribution PDF shows  
561 linear decay in a log-scaled plot (Bracco and others, 2000; Rampal and others, 2009). The dotted line in  
562 Fig. 12b and e shows the best-fit exponential distribution from a random sample of 1000 observations for  
563 both drift components (exponential distributions are only defined for positive values; we fit the function  
564 to the absolute values and scaled by 0.5 so the PDF normalizes to 1). Using a KS-test and bootstrapping  
565 on the remaining observations, we find no significant difference between the exponential distribution and

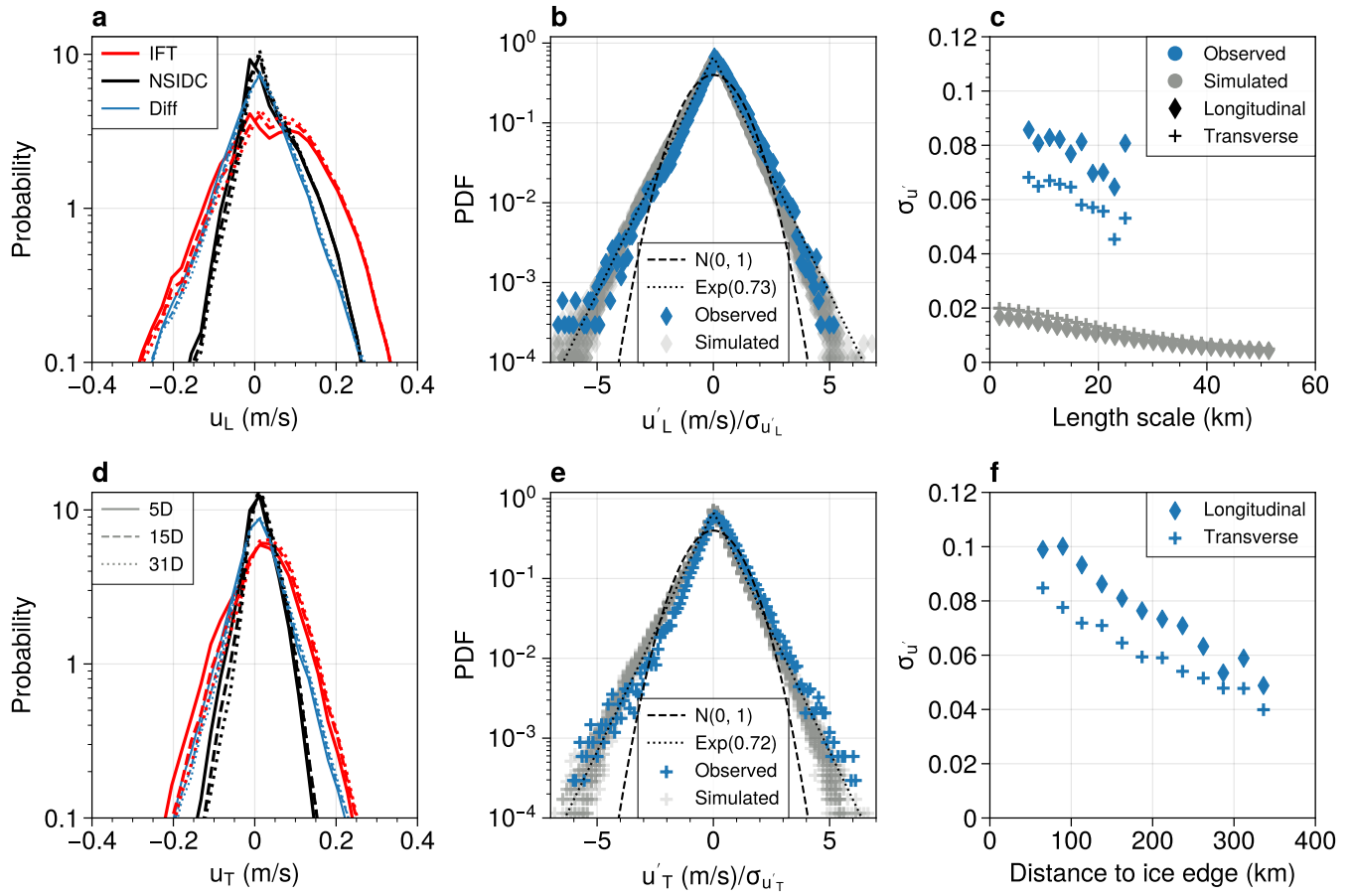


**Fig. 12.** Empirical PDFs of longitudinal (a) and transverse (d) components of daily ice motion for IFT (red), NSIDC (black), and IFT-NSIDC (blue) relative to the mean flow vector calculated over a centered window of  $\tau = 5, 15$ , and  $31$  days (solid, dashed, and dotted lines), shown on left. Positive values of  $u_L$  and  $u_T$  indicate magnitude of the drift vector projection in the direction of the mean flow and  $90^\circ$  to the right of the mean flow, respectively. Center column: Observed IFT (blue) and simulated (gray) empirical PDFs of the longitudinal (b) and transverse (e) components of the drift anomalies scaled by the sample standard deviation. Longitudinal and transverse components were calculated relative to the 5-day centered average NSIDC ice motion. Dashed lines show an equivalent normal distribution (mean=0, standard deviation 1) and dotted lines show a fitted exponential distribution. Note that the fitted exponential is reflected about  $x = 0$ , as the domain of the exponential PDF is strictly non-negative. Right column: (c) Standard deviation of drift anomalies as a function of floe length scale. (d) Standard deviation of drift anomalies as a function of edge distance. As the simulations were performed in a homogeneous eddy field, there is no comparison simulation value here.

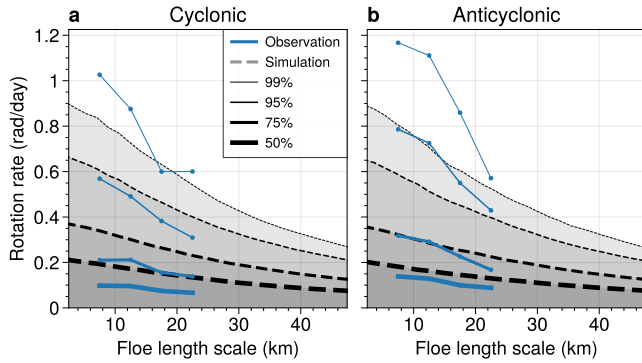


**Fig. 13.** Observed (IFT, blue lines) and simulated (gray shading, black dashed lines) rotation rate percentiles versus floe length scale. Observation percentiles are calculated within 5 km length scale bins. Only bins with at least 100 observations are shown. Lines from thickest to thinnest indicates the 50th, 75th, 95th, and 99th percentiles.

the observed drift perturbations. Thus, the simulation results show that purely eddy-driven ice motion can produce the observed scaled drift anomalies distribution. Note that model experiments suggest that a stochastic wind field and interacting sea ice floes can also produce realistic non-Gaussian sea ice motion distributions (Shaddy and others, 2025).

The influence of ocean eddies on sea ice depends on the link between floe size and eddy size (Brenner and others, 2023; Kim and others, 2024). In both the observations and the simulations, we find that  $\sigma_{u'}$  decreases as the floe size increases (Fig. 12c). The standard deviation of the sea ice motion components is much higher in the observations than in the simulation. One contributor to the difference may be the influence of the fluctuating wind field. Underestimation of ocean turbulence may also be a contributor. To that end, it is worth noting that the QG model was tuned to turbulence in the Beaufort Gyre (Manucharyan and others, 2022). Higher eddy kinetic energy in the Greenland Sea may result in larger sea ice drift variability (Wang and others, 2020).

Spatial variability in sea ice motion depends on the local FSD and on its relationship to the region boundaries. The QG model simulates a homogeneous ocean, thus the simulations cannot explore the spatial effects. However, from the observations (Fig. 12f), we see a strong dependence of  $\sigma_{u'}$  on the proximity of the sea ice edge. This suggests that the role of eddies in sub-grid sea ice variability increases toward the ice edge, which is consistent with known factors for eddy generation in the MIZ (Kozlov and Atadzhanova, 2021; Piccolo and others, 2024).

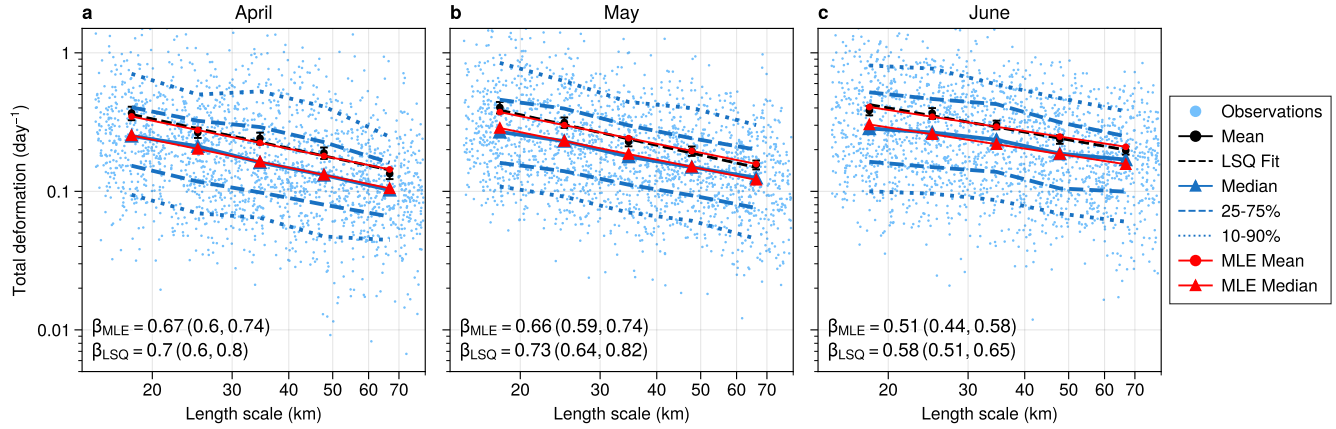


**Fig. 14.** Total deformation rate as a function of polygon length scale ( $L = \sqrt{A_{triangle}}$ ) for months with sufficient data. Blue dots show the stratified random sample. Blue lines show the binned percentile-based statistics (10th, 25th, 50th, 75th, and 90th percentile), while black dots show the bin averages. Whiskers on the black dots show the 95% confidence interval for the mean. Red triangles and dots show the analytical median and mean using the best-fit scaling parameter.

## 584 Rotation rates

585 The ability of IFT to resolve sea ice rotation is a key advancement for remote sensing of sea ice motion  
 586 (Lopez-Acosta, 2021; Manucharyan and others, 2022). In the algorithm, rotation rates are available for a  
 587 subset of tracked floes (those observed by the same satellite on consecutive days). Nonetheless, the number  
 588 is sufficient to examine the relationship between floe size and rotation.

589 In both the simulations and the observations, we see a narrowing of the rotation rate distribution as  
 590 floe size increases (Figure 13). The highest rotation rates are seen in the smallest floes. Smaller floes have  
 591 lower inertia and thus respond more quickly to oceanic forcing (Manucharyan and others, 2022; Kim and  
 592 others, 2024). In addition, the relationship between ocean vorticity and floe size depends on the relative  
 593 size scales of ocean eddies and sea ice floes (Kim and others, 2024). The lower rotation rates of large  
 594 floes may then reflect the ocean currents varying over smaller scales than the size of the floe (Brenner and  
 595 others, 2023). The observed rotation rate distributions, while showing a similar scale dependence as the  
 596 simulations, have narrower peaks and wider tails. One reason may be that the floe observations are not  
 597 limited to low sea ice concentrations. We hypothesize that the narrow peak indicates constraints on the  
 598 rotation rate from floe interactions, while the wider tails arise from the more energetic eddy field in the  
 599 Greenland Sea compared to the simulations.

## 600 Deformation length scales

601 We next examine the spatial variation in sea ice motion by analyzing deformation. Total deformation  $D$   
602 decreases with increasing polygon length scale (Figure 14). Estimated length scale parameters using the  
603 MLE method are  $\beta = 0.67$  in April,  $\beta = 0.66$  in May, and  $\beta = 0.51$  in June (bootstrap 95% confidence  
604 intervals are shown in the figure). Values of  $\beta$  estimated using the least squares (LSQ) method are slightly  
605 higher in each month (0.7, 0.73, and 0.58, respectively), but the differences between the LSQ and MLE  
606 methods are not significant. The decrease in  $\beta$  in June is statistically significant for both MLE and LSQ  
607 methods. It primarily represents an increase in  $D$  at length scales above 25 km, with small changes for the  
608 smallest length scale bin (mean  $L = 18$  km) and an increase from  $0.13 \text{ day}^{-1}$  to  $0.19 \text{ day}^{-1}$  at the largest  
609 length scale bin (mean  $L = 66$  km). Thus, through the melt season, the total deformation rate increases,  
610 while the deformation becomes less localized. **The decrease in the localization of the deformation rates**  
611 **occurs during while the FSD steepens.** Future work should examine the correspondence between the FSD  
612 and deformation properties.

613 These scaling parameters are much steeper than has been observed in the central Arctic winter pack  
614 ice (e.g.,  $\beta = 0.21$  in Hutchings and others (2012, 2018) and  $\beta = 0.2$  in Marsan and others (2004)), and  
615 are similar to the values found for small length scales during the N-ICE 2015 expedition by Oikkonen and  
616 others (2017) for sea ice north of the Fram Strait. In particular, the N-ICE2015 data show  $\beta$  increasing  
617 from 0.52 to 0.82 as the time interval decreased from 24 hours to 10 minutes, and found lower deformation  
618 rates as the distance from the ice edge increased. Our data is primarily concentrated further south than  
619 the N-ICE2015 study location, which may contribute to the difference in observed scaling parameters as  
620 the sea ice properties vary with latitude.

621 The strong agreement between the lognormal MLE and the LSQ results gives confidence in the approach.  
622 The analytically derived lognormal mean and median agree very well with the empirical estimates. One  
623 advantage of the MLE approach is that a larger fraction of the data can be used directly in the estimation,  
624 in contrast to a fit to a small number of bin averages used in the LSQ approach. Assessment of the  
625 lognormality of the data with the MLE  $\beta$  parameters via qq-plots showed good agreement between the  
626 scaled data and the theoretical percentiles of the log-normal distribution. **We also note that the good**  
627 **performance of the MLE fit for the moderate length scales analyzed here does not imply that sea ice**  
628 **deformation is self-similar across all length scales (Hutchings and others, 2024).**

## 629 CONCLUSIONS

630 The floe-scale observations presented here constitute a new class of observations for the spring and sum-  
631 mer MIZ, complementing existing in situ and remote sensing techniques by increasing the sample size of  
632 floe-scale displacement data in the MIZ relative to available drifting buoy observations, by linking floe  
633 shapes with ice dynamics, and by producing floe rotation rates. The ability to resolve rotation is a key  
634 advancement for remote sensing of ice motion, opening new opportunities for research. For example, the  
635 rotation rate data can be used to estimate the underlying ocean vorticity. Notably, the IFT observations  
636 allow simultaneous analysis of the FSD and drift variability. These observations fill a gap in the observa-  
637 tional network, providing data in a season and location where other observations are lacking or have high  
638 uncertainty—specifically, during the melt season.

639 Analysis of the FSD across 18 years of data from the spring-summer transition demonstrates a seasonally  
640 evolving FSD. We investigated the structure of the FSD and found that an exponentially truncated power  
641 law distribution was better supported by the data than standard power law or lognormal distribution.  
642 These spatially extensive, long-term observations of the FSD provide a new angle to characterize the  
643 seasonal evolution of the MIZ, complementing existing remote-sensing derived metrics based on SIC.

644 Building on our prior work, we provide observational and model-based evidence that the variability of  
645 both the sea ice drift anomalies and rotation rates are related to the floe size. In particular, as floe size  
646 increases, the scale of the drift speed anomaly and rotation rate distributions decreases. The simulations  
647 show that the observed scale dependence can arise from ocean turbulence in the absence of winds and large-  
648 scale currents. Future work should weigh the relative roles of wind and ocean forcing in the development  
649 of the drift speed anomaly distribution.

650 This study marks the first time, to our knowledge, that the deformation length scales parameter in  
651 the MIZ has been calculated using floe-scale remote sensing observations. Notably, the deformation scale  
652 dependence is stronger than in the central Arctic and varies seasonally. Deformation rates increase during  
653 the spring season, and the scale dependence of the deformation rates varies by month. Future work will  
654 examine the connection between area-average deformation properties and granular flow, in particular the  
655 potential of identifying differences in deformation rates for strongly and weakly interacting sea ice fields.

656 A major motivation of the work presented here is to enable model development, including new parame-  
657 terizations of FSD effects in sea ice models and representation of mesoscale and submesoscale sea ice-ocean

658 interactions. In particular, the data presented here is anticipated to provide new avenues for evaluating  
659 FSD-dependent ice dynamics in both continuous and discrete element sea ice models.

## 660 ACKNOWLEDGEMENTS

661 DMW, JKH, and MMW were supported by NASA The Science of Terra, Aqua, and Suomi-NPP Pro-  
662 gram (20-TASNPP20-0202, 80NSSC22K062). EMB, MK, and MMW were supported by Office of Naval  
663 Research (ONR) Arctic Program (N00014-20-1-2753, N00014-22-1-2741, and N00014-22-1-2722) and the  
664 ONR Multidisciplinary University Research Initiatives Program (N00014-23-1-2014). MK and MMW were  
665 supported by the ONR Young Investigator Program (N00014-24-1-2283).

666 We acknowledge the use of MODIS True Color and False Color Corrected Reflectance imagery from the  
667 *Terra* and *Aqua* satellites acquired via the from the Worldview Snapshots application, part of the Earth  
668 Observing System Data and Information System (EOSDIS) URL: <https://wvs.earthdata.nasa.gov>.

## 669 REFERENCES

- 670 Afanasyeva E, Alekseeva T, Sokolova J, Demchev D, Chufarova M, Bychenkov YuD and Devyataev O (2019) AARI  
671 Methodology for Sea Ice Charts Composition. *Russian Arctic* (doi: 10.24411/2658-4255-2019-10071)
- 672 Alstott J, Bullmore E and Plenz D (2014) Powerlaw: A Python Package for Analysis of Heavy-Tailed Distributions.  
673 *PLoS ONE*, **9**(1), e85777, ISSN 1932-6203 (doi: 10.1371/journal.pone.0085777)
- 674 Arbic BK, Scott RB, Flierl GR, Morten AJ, Richman JG and Shriver JF (2012) Nonlinear Cascades of Surface  
675 Oceanic Geostrophic Kinetic Energy in the Frequency Domain\*. *Journal of Physical Oceanography*, **42**(9), 1577–  
676 1600, ISSN 0022-3670, 1520-0485 (doi: 10.1175/JPO-D-11-0151.1)
- 677 Åström JA and Polojärvi A (2024) High-Resolution Fracture Dynamics Simulation of Pack-Ice and Drift-Ice For-  
678 mation During Sea Ice Break up Events Using the HiDEM2.0 Code. *Geophysical Research Letters*, **51**(18),  
679 e2024GL110552, ISSN 0094-8276, 1944-8007 (doi: 10.1029/2024GL110552)
- 680 Bateson AW, Feltham DL, Schröder D, Hosekova L, Ridley JK and Aksenov Y (2020) Impact of sea ice floe size  
681 distribution on seasonal fragmentation and melt of Arctic sea ice. *The Cryosphere*, **14**(2), 403–428, ISSN 1994-0424  
682 (doi: 10.5194/tc-14-403-2020)
- 683 Bauke H (2007) Parameter estimation for power-law distributions by maximum likelihood methods. *The European  
684 Physical Journal B*, **58**(2), 167–173, ISSN 1434-6028, 1434-6036 (doi: 10.1140/epjb/e2007-00219-y)

- 685 Blockley E, Vancoppenolle M, Hunke E, Bitz C, Feltham D, Lemieux JF, Losch M, Maisonnave E, Notz D, Rampal  
686 P, Tietsche S, Tremblay B, Turner A, Massonnet F, Ólason E, Roberts A, Aksenov Y, Fichefet T, Garric G, Iovino  
687 D, Madec G, Rousset C, Salas Y Melia D and Schroeder D (2020) The Future of Sea Ice Modeling: Where Do We  
688 Go from Here? *Bulletin of the American Meteorological Society*, **101**(8), E1304–E1311, ISSN 0003-0007, 1520-0477  
689 (doi: 10.1175/BAMS-D-20-0073.1)
- 690 Bouchat A and Tremblay B (2020) Reassessing the Quality of Sea-Ice Deformation Estimates Derived From the  
691 RADARSAT Geophysical Processor System and Its Impact on the Spatiotemporal Scaling Statistics. *Journal of*  
692 *Geophysical Research*, **125**(e2019JC015944), 29
- 693 Boutin G, Williams T, Rampal P, Olason E and Lique C (2021) Wave-sea-ice interactions in a brittle rheological  
694 framework. *The Cryosphere*, **15**(1), 431–457, ISSN 1994-0424 (doi: 10.5194/tc-15-431-2021)
- 695 Bracco A, LaCasce JH and Provenzale A (2000) Velocity Probability Density Functions for Oceanic Floats. *Journal*  
696 *of Physical Oceanography*, **30**(3), 461–474, ISSN 0022-3670, 1520-0485 (doi: 10.1175/1520-0485(2000)030<0461:  
697 VPDFFO>2.0.CO;2)
- 698 Brenner S and Horvat C (2024) Scaling Simulations of Local Wind-Waves Amid Sea Ice Floes. *Journal of Geophysical*  
699 *Research: Oceans*, **129**(12), e2024JC021629, ISSN 2169-9275, 2169-9291 (doi: 10.1029/2024JC021629)
- 700 Brenner S, Horvat C, Hall P, Lo Piccolo A, Fox-Kemper B, Labb   S and Dansereau V (2023) Scale-Dependent Air-  
701 Sea Exchange in the Polar Oceans: Floe-Floe and Floe-Flow Coupling in the Generation of Ice-Ocean Boundary  
702 Layer Turbulence. *Geophysical Research Letters*, **50**(23), e2023GL105703, ISSN 0094-8276, 1944-8007 (doi: 10.  
703 1029/2023GL105703)
- 704 Brunette C, Tremblay LB and Newton R (2022) A new state-dependent parameterization for the free drift of sea ice.  
705 *The Cryosphere*, **16**(2), 533–557, ISSN 19940424 (doi: 10.5194/tc-16-533-2022)
- 706 Buckley EM, Ca  uelas L, Timmermans ML and Wilhelmus MM (2024) Seasonal Evolution of the Sea Ice Floe Size  
707 Distribution from Two Decades of MODIS Data (doi: 10.5194/egusphere-2024-89)
- 708 Burroughs S and Tebbens S (2001) Upper-truncated Power Laws in Natural Systems:. *Pure and Applied Geophysics*,  
709 **158**(4), 741–757, ISSN 0033-4533 (doi: 10.1007/PL00001202)
- 710 Caflisch RE (1998) Monte Carlo and quasi-Monte Carlo methods. *Acta Numerica*, **7**, 1–49
- 711 Chen J and Korsunsky AM (2021) Why is local stress statistics normal, and strain lognormal? *Materials & Design*,  
712 **198**, 109319, ISSN 02641275 (doi: 10.1016/j.matdes.2020.109319)
- 713 Clauset A, Shalizi CR and Newman MEJ (2009) Power-Law Distributions in Empirical Data. *SIAM Review*, **51**(4),  
714 661–703, ISSN 0036-1445, 1095-7200 (doi: 10.1137/070710111)

- 715 Cole ST, Toole JM, Lele R, Timmermans ML, Gallaher SG, Stanton TP, Shaw WJ, Hwang B, Maksym T, Wilkin-  
716 son JP, Ortiz M, Gruber H, Rainville L, Petty AA, Farrell SL, Richter-Menge JA and Haas C (2017) Ice and  
717 ocean velocity in the Arctic marginal ice zone: Ice roughness and momentum transfer. *Elementa: Science of the*  
718 *Anthropocene*, **5**, 55, ISSN 2325-1026 (doi: 10.1525/elementa.241)
- 719 Damsgaard A, Adcroft A and Sergienko O (2018) Application of Discrete Element Methods to Approximate Sea Ice  
720 Dynamics. *Journal of Advances in Modeling Earth Systems*, **10**(9), 2228–2244, ISSN 1942-2466, 1942-2466 (doi:  
721 10.1029/2018MS001299)
- 722 Dedrick K, Partington K, Van Woert M, Bertoia C and Benner D (2001) U.S. National/Naval Ice Center Digital  
723 Sea Ice Data and Climatology. *Canadian Journal of Remote Sensing*, **27**(5), 457–475, ISSN 0703-8992, 1712-7971  
724 (doi: 10.1080/07038992.2001.10854887)
- 725 Dierking W, Stern HL and Hutchings JK (2020) Estimating statistical errors in retrievals of ice velocity and de-  
726 formation parameters from satellite images and buoy arrays. *The Cryosphere*, **14**, 2999–3016 (doi: 10.5194/  
727 tc-14-2999-2020)
- 728 Dumont D (2022) Marginal ice zone dynamics: History, definitions and research perspectives. *Philosophical Trans-  
729 actions of the Royal Society A: Mathematical, Physical and Engineering Sciences*, **380**(2235), 20210253, ISSN  
730 1364-503X, 1471-2962 (doi: 10.1098/rsta.2021.0253)
- 731 Feltham DL (2005) Granular flow in the marginal ice zone. *Philosophical Transactions of the Royal Society A:  
732 Mathematical, Physical and Engineering Sciences*, **363**(1832), 1677–1700, ISSN 1364-503X, 1471-2962 (doi: 10.  
733 1098/rsta.2005.1601)
- 734 Fetterer F, Knowles K, Meier W, Savoie M and Windnagel AK (2017) Sea Ice Index, Version 3. [Northern Hemisphere].  
735 Boulder, Colorado USA. NSIDC: National Snow and Ice Data Center (doi: 10.7265/N5K072F8)
- 736 Gabrielski A, Badin G and Kaleschke L (2015) Anomalous dispersion of sea ice in the Fram Strait region. *Journal  
737 of Geophysical Research: Oceans*, **120**(3), 1809–1824 (doi: 10.1002/2014JC010359)
- 738 Gerland S, Barber D, Meier W, Mundy CJ, Holland M, Kern S, Li Z, Michel C, Perovich DK and Tamura T (2019)  
739 Essential gaps and uncertainties in the understanding of the roles and functions of Arctic sea ice. *Environmental  
740 Research Letters*, **14**(4), 1–14, ISSN 1748-9326 (doi: 10.1088/1748-9326/ab09b3)
- 741 Girard L, Bouillon S, Weiss J, Amitrano D, Fichefet T and Legat V (2011) A new modeling framework for sea-ice  
742 mechanics based on elasto-brittle rheology. *Annals of Glaciology*, **52**(57 PART 1), 123–132, ISSN 02603055 (doi:  
743 10.3189/172756411795931499)

- 744 Girard-Ardhuin F and Ezraty R (2012) Enhanced Arctic Sea Ice Drift Estimation Merging Radiometer and Scatterometer Data. *IEEE Transactions on Geoscience and Remote Sensing*, **50**(7), 2639–2648, ISSN 0196-2892, 1558-0644  
745 (doi: 10.1109/TGRS.2012.2184124)
- 746
- 747 Goldstein ML, Morris SA and Yen GG (2004) Problems with fitting to the power-law distribution. *The European Physical Journal B*, **41**(2), 255–258, ISSN 1434-6028, 1434-6036 (doi: 10.1140/epjb/e2004-00316-5)
- 748
- 749 Gui D, Lei R, Pang X, Hutchings JK, Zuo G and Zhai M (2020) Validation of remote-sensing products of sea-ice motion: A case study in the western Arctic Ocean. *Journal of Glaciology*, **66**(259), 807–821, ISSN 00221430 (doi:  
750 10.1017/jog.2020.49)
- 751
- 752 Gupta M, Gürcan E and Thompson AF (2024) Eddy-Induced Dispersion of Sea Ice Floes at the Marginal Ice Zone. *Geophysical Research Letters*, **51**(2), e2023GL105656, ISSN 0094-8276, 1944-8007 (doi: 10.1029/2023GL105656)
- 753
- 754 Hakkinen S (1987) Feedback between ice flow, barotropic flow, and baroclinic flow in the presence of bottom  
755 topography. *Journal of Geophysical Research: Oceans*, **92**(C4), 3807–3820, ISSN 0148-0227 (doi: 10.1029/  
756 JC092iC04p03807)
- 757 Hatcher S, Ahmed A, Kim M and Wilhelmus MM (2022) SOIT: Satellite overpass identification tool. Zenodo (doi:  
758 10.5281/zenodo.6475619)
- 759 Heorton HDBS, Feltham DL and Tsamados M (2018) Stress and deformation characteristics of sea ice in a high-  
760 resolution, anisotropic sea ice model. *Philosophical Transactions of the Royal Society A: Mathematical, Physical  
761 and Engineering Sciences*, **376**(2129), 20170349, ISSN 1364-503X, 1471-2962 (doi: 10.1098/rsta.2017.0349)
- 762 Herman A (2010) Sea-ice floe-size distribution in the context of spontaneous scaling emergence in stochastic systems.  
763 *Physical Review E*, **81**(066123), 1–5, ISSN 1539-3755, 1550-2376 (doi: 10.1103/PhysRevE.81.066123)
- 764 Herman A (2022) Granular effects in sea ice rheology in the marginal ice zone. *Philosophical Transactions of the Royal  
765 Society A: Mathematical, Physical and Engineering Sciences*, **380**(2235), 20210260, ISSN 1364-503X, 1471-2962  
766 (doi: 10.1098/rsta.2021.0260)
- 767 Hibler WD (1979) A Dynamic Thermodynamic Sea Ice Model. *Journal of Physical Oceanography*, **9**(4), 815–846,  
768 ISSN 0022-3670 (doi: 10.1175/1520-0485(1979)009<0815:ADTSIM>2.0.CO;2)
- 769 Horvat C (2022) Floes, the marginal ice zone and coupled wave-sea-ice feedbacks. *Philosophical Transactions of  
770 the Royal Society A: Mathematical, Physical and Engineering Sciences*, **380**(2235), 20210252, ISSN 1364-503X,  
771 1471-2962 (doi: 10.1098/rsta.2021.0252)
- 772 Horvat C and Tziperman E (2015) A prognostic model of the sea-ice floe size and thickness distribution. *The  
773 Cryosphere*, **9**(6), 2119–2134, ISSN 1994-0424 (doi: 10.5194/tc-9-2119-2015)

- 774 Horvat C, Tziperman E and Campin JM (2016) Interaction of sea ice floe size, ocean eddies, and sea ice melting.  
775 *Geophysical Research Letters*, **43**(15), 8083–8090 (doi: 10.1002/2016GL069742)
- 776 Hunke EC and Dukowicz JK (1997) An Elastic–Viscous–Plastic Model for Sea Ice Dynamics. *Journal of Physical*  
777 *Oceanography*, **27**(9), 1849–1867, ISSN 0022-3670, 1520-0485 (doi: 10.1175/1520-0485(1997)027<1849:AEVPMF>  
778 2.0.CO;2)
- 779 Hutchings JK, Roberts A, Geiger CA and Richter-Menge J (2011) Spatial and temporal characterization of sea-ice  
780 deformation. *Annals of Glaciology*, **52**(57 PART 2), 360–368, ISSN 02603055 (doi: 10.3189/172756411795931769)
- 781 Hutchings JK, Heil P, Steer A and Hibler WD (2012) Subsynoptic scale spatial variability of sea ice deformation in  
782 the western Weddell Sea during early summer. *Journal of Geophysical Research*, **117**(C1), C01002, ISSN 0148-0227  
783 (doi: 10.1029/2011JC006961)
- 784 Hutchings JK, Roberts A, Geiger CA and Richter-Menge J (2018) Corrigendum: Spatial and temporal characterisa-  
785 tion of sea-ice deformation. *Journal of Glaciology*, **64**(244), 343–346, ISSN 00221430 (doi: 10.1017/jog.2018.11)
- 786 Hutchings JK, Bliss AC, Mondal D and Elosegui P (2024) Sea Ice Deformation Is Not Scale Invariant Over Length  
787 Scales Greater Than a Kilometer. *Geophysical Research Letters*, **51**(12), e2024GL108582, ISSN 0094-8276, 1944-  
788 8007 (doi: 10.1029/2024GL108582)
- 789 Hutter N, Losch M and Menemenlis D (2018) Scaling Properties of Arctic Sea Ice Deformation in a High-Resolution  
790 Viscous-Plastic Sea Ice Model and in Satellite Observations. *Journal of Geophysical Research: Oceans*, **123**(1),  
791 672–687, ISSN 2169-9275, 2169-9291 (doi: 10.1002/2017JC013119)
- 792 Hutter N, Bouchat A, Dupont F, Dukhovskoy D, Koldunov N, Lee YJ, Lemieux JF, Lique C, Losch M, Maslowski  
793 W, Myers PG, Ólason E, Rampal P, Rasmussen T, Talandier C, Tremblay B and Wang Q (2022) Sea Ice Rheology  
794 Experiment (SIREx): 2. Evaluating Linear Kinematic Features in High-Resolution Sea Ice Simulations. *Journal of*  
795 *Geophysical Research: Oceans*, **127**(4), e2021JC017666, ISSN 2169-9275, 2169-9291 (doi: 10.1029/2021JC017666)
- 796 Hwang B (2013) Inter-comparison of satellite sea ice motion with drifting buoy data. *International Journal of Remote  
797 Sensing*, **34**(24), 8741–8763, ISSN 0143-1161, 1366-5901 (doi: 10.1080/01431161.2013.848309)
- 798 Hwang B, Wilkinson J, Maksym T, Gruber HC, Schweiger A, Horvat C, Perovich DK, Arntsen AE, Stanton TP, Ren  
799 J and Wadhams P (2017) Winter-to-summer transition of Arctic sea ice breakup and floe size distribution in the  
800 Beaufort Sea. *Elementa: Science of the Anthropocene*, **5**, 40, ISSN 2325-1026 (doi: 10.1525/elementa.232)
- 801 Itkin P, Spreen G, Cheng B, Doble M, Girard-Ardhuin F, Haapala J, Hughes N, Kaleschke L, Nicolaus M and  
802 Wilkinson J (2017) Thin ice and storms: Sea ice deformation from buoy arrays deployed during N-ICE2015.  
803 *Journal of Geophysical Research: Oceans*, **122**(6), 4661–4674, ISSN 21699275 (doi: 10.1002/2016JC012403)

- 804 Johannessen JA, Johannessen OM, Svendsen E, Shuchman R, Manley T, Campbell WJ, Josberger EG, Sandven S,  
805 Gascard JC, Olaussen T, Davidson K and Van Leer J (1987a) Mesoscale eddies in the Fram Strait marginal ice  
806 zone during the 1983 and 1984 Marginal Ice Zone Experiments. *Journal of Geophysical Research*, **92**(C7), 6754,  
807 ISSN 0148-0227 (doi: 10.1029/JC092iC07p06754)
- 808 Johannessen OM, Johannessen JA, Svendsen E, Shuchman RA, Campbell WJ and Josberger E (1987b) Ice-Edge  
809 Eddies in the Fram Strait Marginal Ice Zone. *Science*, **236**(4800), 427–429 (doi: 10.1126/science.236.4800.427)
- 810 Kim M, Manucharyan GE and Wilhelmus MM (2024) Characterization of sea ice kinematics over oceanic eddies (doi:  
811 10.48550/arXiv.2411.12926)
- 812 Kozlov IE and Atadzhanova OA (2021) Eddies in the Marginal Ice Zone of Fram Strait and Svalbard from Spaceborne  
813 SAR Observations in Winter. *Remote Sensing*, **14**(1), 134, ISSN 2072-4292 (doi: 10.3390/rs14010134)
- 814 Kwok R, Curlander J, McConnell R and Pang S (1990) An ice-motion tracking system at the Alaska SAR facility.  
815 *IEEE Journal of Oceanic Engineering*, **15**(1), 44–54, ISSN 03649059 (doi: 10.1109/48.46835)
- 816 Kwok R, Schweiger A, Rothrock DA, Pang S and Kottmeier C (1998) Sea ice motion from satellite passive microwave  
817 imagery assessed with ERS SAR and buoy motions. *Journal of Geophysical Research: Oceans*, **103**(C4), 8191–8214,  
818 ISSN 0148-0227 (doi: 10.1029/97JC03334)
- 819 Kwok R, Cunningham GF and Hibler WD (2003) Sub-daily sea ice motion and deformation from RADARSAT  
820 observations: SHORT PERIOD ICE MOTION. *Geophysical Research Letters*, **30**(23), n/a–n/a, ISSN 00948276  
821 (doi: 10.1029/2003GL018723)
- 822 Lavergne T, Eastwood S, Teffah Z, Schyberg H and Breivik LA (2010) Sea ice motion from low-resolution satel-  
823 lite sensors: An alternative method and its validation in the Arctic. *Journal of Geophysical Research: Oceans*,  
824 **115**(C10), 032 (doi: 10.1029/2009JC005958)
- 825 Leppäranta M (2011) *The Drift of Sea Ice*. Springer Praxis Books, Springer-Verlag Berlin Heidelberg, 2 edition, ISBN  
826 978-3-642-04682-7
- 827 Lindsay RW and Stern HL (2003) The RADARSAT Geophysical Processor System: Quality of sea ice trajectory and  
828 deformation estimates. *Journal of Atmospheric and Oceanic Technology*, **20**(9), 1333–1347, ISSN 07390572 (doi:  
829 10.1175/1520-0426(2003)020<1333:TRGPSQ>2.0.CO;2)
- 830 Loose B, McGillis WR, Perovich D, Zappa CJ and Schlosser P (2014) A parameter model of gas exchange for the  
831 seasonal sea ice zone. *Ocean Science*, **10**(1), 17–28, ISSN 1812-0792 (doi: 10.5194/os-10-17-2014)
- 832 Lopez-Acosta R (2021) *Sea Ice Drift in Arctic Marginal Ice Zones Derived from Optical Satellite Imagery*. Ph.D.  
833 thesis, University of California Riverside, Riverside, CA

- 834 Lopez-Acosta R, Schodlok MP and Wilhelmus MM (2019) Ice Floe Tracker: An algorithm to automatically re-  
835 trive Lagrangian trajectories via feature matching from moderate-resolution visual imagery. *Remote Sensing of*  
836 *Environment*, **234**(111406), 1–15, ISSN 00344257 (doi: 10.1016/j.rse.2019.111406)
- 837 Lu P, Li ZJ, Zhang ZH and Dong XL (2008) Aerial observations of floe size distribution in the marginal ice zone  
838 of summer Prydz Bay. *Journal of Geophysical Research: Oceans*, **113**(C2), 2006JC003965, ISSN 0148-0227 (doi:  
839 10.1029/2006JC003965)
- 840 Manley TO (1987) Effects of sub-ice mesoscale features within the marginal ice zone of Fram Strait. *Journal of*  
841 *Geophysical Research: Oceans*, **92**(C4), 3944–3960, ISSN 0148-0227 (doi: 10.1029/JC092iC04p03944)
- 842 Manucharyan GE and Montemuro BP (2022) SubZero: A Sea Ice Model With an Explicit Representation of the Floe  
843 Life Cycle. *Journal of Advances in Modeling Earth Systems*, **14**(12), e2022MS003247, ISSN 1942-2466, 1942-2466  
844 (doi: 10.1029/2022MS003247)
- 845 Manucharyan GE, Lopez-Acosta R and Wilhelmus MM (2022) Spinning ice floes reveal intensification of mesoscale  
846 eddies in the western Arctic Ocean. *Scientific Reports*, **12**(7070) (doi: 10.1038/s41598-022-10712-z)
- 847 Marsan D, Stern H, Lindsay R and Weiss J (2004) Scale dependence and localization of the deformation of arctic  
848 sea ice. *Physical Review Letters*, **93**(17), 3–6, ISSN 00319007 (doi: 10.1103/PhysRevLett.93.178501)
- 849 McNutt SL and Overland JE (2003) Spatial hierarchy in Arctic sea ice dynamics. *Tellus A: Dynamic Meteorology*  
850 and *Oceanography*, **55**(2), 181–191 (doi: 10.3402/tellusa.v55i2.12088)
- 851 Meier WN and Dai M (2006) High-resolution sea-ice motions from AMSR-E imagery. *Annals of Glaciology*, **44**,  
852 352–356, ISSN 0260-3055, 1727-5644 (doi: 10.3189/172756406781811286)
- 853 Meier WN, Fetterer F, Windnagel AK and Stewart S (2021) NOAA / NSIDC Climate Data Record of Passive  
854 Microwave Sea Ice Concentration, Version 4
- 855 Meier WN, Stewart JS, Windnagel A and Fetterer FM (2022) Comparison of Hemispheric and Regional Sea Ice  
856 Extent and Area Trends from NOAA and NASA Passive Microwave-Derived Climate Records. *Remote Sensing*,  
857 **14**(3), ISSN 20724292 (doi: 10.3390/rs14030619)
- 858 Mokus NGA and Montiel F (2022) Wave-triggered breakup in the marginal ice zone generates lognormal floe  
859 size distributions: A simulation study. *The Cryosphere*, **16**(10), 4447–4472, ISSN 1994-0424 (doi: 10.5194/  
860 tc-16-4447-2022)
- 861 Montiel F and Mokus N (2022) Theoretical framework for the emergent floe size distribution in the marginal ice  
862 zone: The case for log-normality. *Philosophical Transactions of the Royal Society A: Mathematical, Physical and*  
863 *Engineering Sciences*, **380**(2235), 20210257, ISSN 1364-503X, 1471-2962 (doi: 10.1098/rsta.2021.0257)

- 864 Morozov EA and Kozlov IE (2023) Eddies in the Arctic Ocean Revealed from MODIS Optical Imagery. *Remote*  
865 *Sensing*, **15**(6), 1608, ISSN 2072-4292 (doi: 10.3390/rs15061608)
- 866 Ninnis RM, Emery WJ and Collins MJ (1986) Automated extraction of pack ice motion from advanced very high  
867 resolution radiometer imagery. *Journal of Geophysical Research: Oceans*, **91**(C9), 10725–10734, ISSN 0148-0227  
868 (doi: 10.1029/JC091iC09p10725)
- 869 Nurser AJG and Bacon S (2014) The Rossby radius in the Arctic Ocean. *Ocean Science*, **10**(6), 967–975 (doi:  
870 10.5194/os-10-967-2014)
- 871 Oikkonen A, Haapala J, Lensu M, Karvonen J and Itkin P (2017) Small-scale sea ice deformation during N-ICE2015:  
872 From compact pack ice to marginal ice zone. *Journal of Geophysical Research: Oceans*, **122**, 5105–5120
- 873 Ólason E, Boutin G, Korosov A, Rampal P, Williams T, Kimmritz M, Dansereau V and Samaké A (2022) A New  
874 Brittle Rheology and Numerical Framework for Large-Scale Sea-Ice Models. *Journal of Advances in Modeling Earth*  
875 *Systems*, **14**(8), e2021MS002685, ISSN 1942-2466, 1942-2466 (doi: 10.1029/2021MS002685)
- 876 Overland JE, Walter BA, Curtin TB and Turet P (1995) Hierarchy and sea ice mechanics: A case study from the  
877 Beaufort Sea. *Journal of Geophysical Research*, **100**(C3), 4559, ISSN 0148-0227 (doi: 10.1029/94JC02502)
- 878 Paget M, Worby AP and Michael KJ (2001) Determining the floe-size distribution of East Antarctic sea ice  
879 from digital aerial photographs. *Annals of Glaciology*, **33**, 94–100, ISSN 0260-3055, 1727-5644 (doi: 10.3189/  
880 172756401781818473)
- 881 Pedregosa F, Varoquaux G, Gramfort A, Michel V, Thirion B, Grisel O, Blondel M, Prettenhofer P, Weiss R,  
882 Dubourg V, Vanderplas J, Passos A and Cournapeau D (2011) Scikit-learn: Machine Learning in Python. *Journal*  
883 *of Machine Learning Resaerch*, **12**, 2825–2830, ISSN 15529924 (doi: 10.1289/EHP4713)
- 884 Piccolo AL, Horvat C and Fox-Kemper B (2024) Energetics and Transfer of Submesoscale Brine Driven Eddies at a  
885 Sea Ice Edge. *Journal of Physical Oceanography*, ISSN 0022-3670, 1520-0485 (doi: 10.1175/JPO-D-23-0147.1)
- 886 Rabe B, Cox CJ, Fang YC, Goessling H, Granskog MA, Hoppmann M, Hutchings JK, Krumpen T, Kuznetsov  
887 I, Lei R, Li T, Maslowski W, Nicolaus M, Perovich D, Persson O, Regnery J, Rigor I, Shupe MD, Sokolov V,  
888 Spreen G, Stanton T, Watkins DM, Blockley E, Buenger HJ, Cole S, Fong A, Haapala J, Heuzé C, Hoppe CJM,  
889 Janout M, Jutila A, Katlein C, Krishfield R, Lin L, Ludwig V, Morgenstern A, O'Brien J, Zurita AQ, Rackow  
890 T, Riemann-Campe K, Rohde J, Shaw W, Smolyanitsky V, Solomon A, Sperling A, Tao R, Toole J, Tsamados  
891 M, Zhu J and Zuo G (2024) The MOSAiC Distributed Network: Observing the coupled Arctic system with  
892 multidisciplinary, coordinated platforms. *Elementa: Science of the Anthropocene*, **12**(1), 00103, ISSN 2325-1026  
893 (doi: 10.1525/elementa.2023.00103)

- 894 Rampal P, Weiss J, Marsan D, Lindsay R and Stern H (2008) Scaling properties of sea ice deformation from  
895 buoy dispersion analysis. *Journal of Geophysical Research: Oceans*, **113**(3), 1–12, ISSN 21699291 (doi: 10.1029/  
896 2007JC004143)
- 897 Rampal P, Weiss J, Marsan D and Bourgoin M (2009) Arctic sea ice velocity field: General circulation and  
898 turbulent-like fluctuations. *Journal of Geophysical Research: Oceans*, **114**(10), 1–17, ISSN 21699291 (doi:  
899 10.1029/2008JC005227)
- 900 Rampal P, Bouillon S, Ólason E and Morlighem M (2016) neXtSIM: A new Lagrangian sea ice model. *The Cryosphere*,  
901 **10**(3), 1055–1073, ISSN 1994-0424 (doi: 10.5194/tc-10-1055-2016)
- 902 Rampal P, Dansereau V, Olason E, Bouillon S, Williams T, Korosov A and Samaké A (2019) On the multi-fractal  
903 scaling properties of sea ice deformation. *The Cryosphere*, **13**(9), 2457–2474, ISSN 1994-0424 (doi: 10.5194/  
904 tc-13-2457-2019)
- 905 Rigor IG, Clemente-Colon P and Hudson E (2008) The international arctic buoy programme (IABP): A cornerstone  
906 of the Arctic observing network. In *OCEANS 2008*, 1–3 (doi: 10.1109/OCEANS.2008.5152136)
- 907 Roach LA, Horvat C, Dean SM and Bitz CM (2018) An Emergent Sea Ice Floe Size Distribution in a Global Coupled  
908 Ocean-Sea Ice Model. *Journal of Geophysical Research: Oceans*, **123**(6), 4322–4337, ISSN 2169-9275, 2169-9291  
909 (doi: 10.1029/2017JC013692)
- 910 Roach LA, Smith MM, Herman A and Ringisen D (2024) Physics of the Seasonal Sea Ice Zone. *Annual Review of  
911 Marine Science*, ISSN 1941-1405, 1941-0611 (doi: 10.1146/annurev-marine-121422-015323)
- 912 Rothrock DA and Thorndike AS (1984) Measuring the sea ice floe size distribution. *Journal of Geophysical Research:  
913 Oceans*, **89**(C4), 6477–6486, ISSN 0148-0227 (doi: 10.1029/JC089iC04p06477)
- 914 Sandven S, Spreen G, Heygster G, Girard-Ardhuin F, Farrell SL, Dierking W and Allard RA (2023) Sea Ice Remote  
915 Sensing—Recent Developments in Methods and Climate Data Sets. *Surveys in Geophysics*, ISSN 0169-3298, 1573–  
916 0956 (doi: 10.1007/s10712-023-09781-0)
- 917 Shaddy B, Greaney PA and Rallabandi B (2025) Wind-driven collisions between floes explain the observed dispersion  
918 of Arctic sea ice (doi: 10.48550/arXiv.2502.17668)
- 919 Smedsrød LH, Halvorsen MH, Stroeve JC, Zhang R and Kloster K (2017) Fram Strait sea ice export variability  
920 and September Arctic sea ice extent over the last 80 years. *The Cryosphere*, **11**(1), 65–79, ISSN 1994-0424 (doi:  
921 10.5194/tc-11-65-2017)
- 922 Spreen G, de Steur L, Divine D, Gerland S, Hansen E and Kwok R (2020) Arctic Sea Ice Volume Export Through Fram  
923 Strait From 1992 to 2014. *Journal of Geophysical Research: Oceans*, **125**(6), 1–16 (doi: 10.1029/2019JC016039)

- 924 Stern HL and Lindsay RW (2009) Spatial scaling of Arctic sea ice deformation. *Journal of Geophysical Research: Oceans*, **114**(10), 1–10, ISSN 21699291 (doi: 10.1029/2009JC005380)
- 925
- 926 Stern HL, Schweiger AJ, Stark M, Zhang J, Steele M and Hwang B (2018a) Seasonal evolution of the sea-ice floe size distribution in the Beaufort and Chukchi seas. *Elementa: Science of the Anthropocene*, **6**, 48, ISSN 2325-1026 (doi: 10.1525/elementa.305)
- 927
- 928
- 929 Stern HL, Schweiger AJ, Zhang J and Steele M (2018b) On reconciling disparate studies of the sea-ice floe size distribution. *Elementa: Science of the Anthropocene*, **6**, 49, ISSN 2325-1026 (doi: 10.1525/elementa.304)
- 930
- 931 Sumata H, Lavergne T, Girard-Ardhuin F, Kimura N, Tschudi MA, Kauker F, Karcher M and Gerdes R (2014) An intercomparison of Arctic ice drift products to deduce uncertainty estimates. *Journal of Geophysical Research: Oceans*, **119**(8), 4887–4921, ISSN 21699275 (doi: 10.1002/2013JC009724)
- 932
- 933
- 934 Sumata H, De Steur L, Gerland S, Divine DV and Pavlova O (2022) Unprecedented decline of Arctic sea ice outflow in 2018. *Nature Communications*, **13**(1), 1747, ISSN 2041-1723 (doi: 10.1038/s41467-022-29470-7)
- 935
- 936 Tandon NF, Kushner PJ, Docquier D, Wettstein JJ and Li C (2018) Reassessing Sea Ice Drift and Its Relationship to Long-Term Arctic Sea Ice Loss in Coupled Climate Models. *Journal of Geophysical Research: Oceans*, **123**(6), 4338–4359, ISSN 2169-9275, 2169-9291 (doi: 10.1029/2017JC013697)
- 937
- 938
- 939 Tang A, Liu H, Liu G, Zhong Y, Wang L, Lu Q, Wang J and Shen Y (2020) Lognormal Distribution of Local Strain: A Universal Law of Plastic Deformation in Material. *Physical Review Letters*, **124**(15), 155501, ISSN 0031-9007, 1079-7114 (doi: 10.1103/PhysRevLett.124.155501)
- 940
- 941
- 942 Thorndike AS and Colony R (1982) Sea ice motion in response to geostrophic winds. *Journal of Geophysical Research*, **87**(C8), 5845, ISSN 0148-0227 (doi: 10.1029/JC087iC08p05845)
- 943
- 944 Toyota T, Takatsuji S and Nakayama M (2006) Characteristics of sea ice floe size distribution in the seasonal ice zone. *Geophysical Research Letters*, **33**(2), 2005GL024556, ISSN 0094-8276, 1944-8007 (doi: 10.1029/2005GL024556)
- 945
- 946 Tsamados M, Feltham DL and Wilchinsky AV (2013) Impact of a new anisotropic rheology on simulations of Arctic sea ice. *Journal of Geophysical Research: Oceans*, **118**(February 2012), 91–107 (doi: 10.1029/2012JC007990)
- 947
- 948 Tschudi MA, Meier WN and Stewart JS (2020) An enhancement to sea ice motion and age products at the National Snow and Ice Data Center (NSIDC). *The Cryosphere*, **14**(5), 1519–1536, ISSN 1994-0424 (doi: 10.5194/tc-14-1519-2020)
- 949
- 950
- 951 Uttal T, Curry JA, McPhee MG, Perovich DK, Moritz RE, Maslanik JA, Guest PS, Stern HL, Moore JA, Turenne R, Heiberg A, Serreze MC, Wylie DP, Persson OG, Paulson CA, Halle C, Morison JH, Wheeler PA, Makshtas A,
- 952

- 953 Welch H, Shupe MD, Intrieri JM, Stamnes K, Lindsey RW, Pinkel R, Pegau WS, Stanton TP and Grenfeld TC  
954 (2002) Surface Heat Budget of the Arctic Ocean. *Bulletin of the American Meteorological Society*, **83**(2), 255 –  
955 276 (doi: 10.1175/1520-0477(2002)083<0255:SHBOTA>2.3.CO;2)
- 956 Wadhams P (1981) The ice cover in the Greenland and Norwegian seas. *Reviews of Geophysics*, **19**(3), 345–393, ISSN  
957 8755-1209, 1944-9208 (doi: 10.1029/RG019i003p00345)
- 958 Walsh JE, Eicken H, Redilla K and Johnson M (2022) Sea ice breakup and freeze-up indicators for users of the Arctic  
959 coastal environment. *The Cryosphere*, **16**(11), 4617–4635, ISSN 1994-0424 (doi: 10.5194/tc-16-4617-2022)
- 960 Wang Q, Koldunov NV, Danilov S, Sidorenko D, Wekerle C, Scholz P, Bashmachnikov IL and Jung T (2020) Eddy  
961 Kinetic Energy in the Arctic Ocean From a Global Simulation With a 1-km Arctic. *Geophysical Research Letters*,  
962 **47**(14), e2020GL088550, ISSN 0094-8276, 1944-8007 (doi: 10.1029/2020GL088550)
- 963 Wang X, Chen R, Li C, Chen Z, Hui F and Cheng X (2022) An Intercomparison of Satellite Derived Arctic Sea Ice  
964 Motion Products. *Remote Sensing*, **14**(5), 1261, ISSN 2072-4292 (doi: 10.3390/rs14051261)
- 965 Watkins DM, Bliss AC, Hutchings JK and Wilhelmus MM (2023) Evidence of Abrupt Transitions Between Sea Ice  
966 Dynamical Regimes in the East Greenland Marginal Ice Zone. *Geophysical Research Letters*, **50**(e2023GL103558),  
967 1–10
- 968 Webster M, Rigor I and Wright N (2022) Observing Arctic Sea Ice. *Oceanography*, ISSN 10428275 (doi: 10.5670/  
969 oceanog.2022.115)
- 970 Wenta M and Herman A (2018) The influence of the spatial distribution of leads and ice floes on the atmospheric  
971 boundary layer over fragmented sea ice. *Annals of Glaciology*, **59**(76pt2), 213–229, ISSN 02603055 (doi: 10.1017/  
972 aog.2018.15)
- 973 Zhang J (2021) Sea Ice Properties in High-Resolution Sea Ice Models. *Journal of Geophysical Research: Oceans*,  
974 **126**(1), ISSN 2169-9275, 2169-9291 (doi: 10.1029/2020JC016686)
- 975 Zhang J, Schweiger A, Steele M and Stern H (2015) Sea ice floe size distribution in the marginal ice zone: Theory and  
976 numerical experiments. *Journal of Geophysical Research: Oceans*, **120**(5), 3484–3498, ISSN 2169-9275, 2169-9291  
977 (doi: 10.1002/2015JC010770)
- 978 Zhang X, Haapala J and Uotila P (2024) Capacity of a set of CMIP6 models to simulate Arctic sea ice drift. *Annals  
979 of Glaciology*, 1–19, ISSN 0260-3055, 1727-5644 (doi: 10.1017/aog.2024.25)